Substantial π-aromaticity in the anionic heavy-metal cluster [Th@Bi12]4–

Armin R Eulenstein, Yannick J Franzke, Niels Lichtenberger, Robert J Wilson, H Lars Deubner, Florian Kraus, Rodolphe Clérac, Florian Weigend, Stefanie Dehnen

Substantial π-aromaticity in the anionic heavy-metal cluster $[Th@Bi_{12}]^{4-}$

Armin R. Eulenstein[1,2,6], Yannick J. Franzke[3,5,6], Niels Lichtenberger[1,2], Robert J. Wilson[1,2], H. Lars Deubner[1], Florian Kraus[1], Rodolphe Clérac[4], Florian Weigend[1]✉ and Stefanie Dehnen[1,2]✉

[1]Fachbereich Chemie, Philipps-Universität Marburg, Marburg, Germany. [2]Wissenschaftliches Zentrum für Materialwissenschaften (WZMW), Philipps-Universität Marburg, Marburg, Germany. [3]Institute of Physical Chemistry, Karlsruhe Institute of Technology (KIT), Karlsruhe, Germany. [4]Univ. Bordeaux, CNRS, Centre de Recherche Paul Pascal, Pessac, France. [5]Present address: Fachbereich Chemie, Philipps-Universität Marburg, Marburg, Germany. [6]These authors contributed equally: Armin R. Eulenstein, Yannick J. Franzke. ✉e-mail: florian.weigend@chemie.uni-marburg.de; dehnen@chemie.uni-marburg.de

The concept of aromaticity was originally defined as a property of unsaturated, cyclic planar organic molecules like benzene, which gain stability by the inherent delocalization of $4n+2$ π-electrons over the ring atoms. Since then, π-aromaticity has been observed for a large variety of organic and inorganic non-metal compounds, yet, for molecules consisting only of metal atoms, it has remained restricted to systems with three to five atoms. Here, we present the straightforward synthesis of a metal 12-ring that exhibits 2π-aromaticity and has a ring current much stronger than that of benzene (6π) and equivalent to that of porphine (26π), despite these organic molecules having (much) larger numbers of π-electrons. Highly reducing reaction conditions allowed access to the heterometallic anion $[Th@Bi_{12}]^{4-}$, with interstitial Th^{4+} stabilizing a Bi_{12}^{8-} moiety. Our results show that it is possible to design and generate substantial π-aromaticity in large metal rings, and we hope that such π-aromatic heavy-metal cycles will eventually find use in cluster-based reactions.

Aromaticity was originally defined as a property of unsaturated, cyclic planar organic molecules like benzene, which gain stability by inherent delocalization of $4n+2$ π-electrons over the atoms of a highly symmetric ring[1]. This electron delocalization allows a ring current to be sustained in an external magnetic field. In addition to structural and energetic features, as well as specific reactivity patterns, ring currents are used as another aromaticity criterion[2–4], which can be probed experimentally via NMR shifts or calculated by means of quantum chemistry. The latter is possible either directly[5] or indirectly via nucleus-independent chemical shifts (NICSs)[6]. Hückel postulated that all planar monocyclic molecules with $4n+2$ π-electrons fulfil the preconditions for aromaticity, while $4n$ π-electrons lead to antiaromaticity. These rules were then applied to organic monocycles with the general formula C_nR_n (R = H, organic substituent), to heteroaromatic compounds comprising one or more non-carbon atoms in the cycle, as well as to a small number of accessible purely inorganic compounds. The list of experimentally accessible π-aromatic molecules comprising exclusively metal atoms is considerably shorter, although metal atoms should allow for strong electron delocalization of any kind due to their preference for metallic bonding. Yet, only a few planar cyclic compounds with notable ring currents have been reported so far, with a maximum number of five metal atoms, as metal atoms tend to form polyhedral structures rather than cycles. The challenge hence is to overcome these two contradicting preconditions and find a way of stabilizing larger metal cycles, not only to expand the knowledge of this highly uncommon class of compounds, but also to explore and further shape such molecules' exceptional electronic properties and eventually reactivities. Figure 1 provides an overview of the classes of π-aromatic molecules that have been verified experimentally, along with their calculated NICS values (in ppm) and ring current strengths (in nA T^{-1}), thereby indicating all experimentally secured types of molecules exhibiting all-metal π-aromaticity.

In contrast to the large number and diversity of typical π-aromatic C_nH_n cycles (Fig. 1a; including $Li_2[(Me_3SiC)_4]$ as a rare example of four-membered cycles[7]) and heteroaromatic analogues (Fig. 1b; including derivatives like $K[(B^tBu)_2CCH(SiMe_3)_2]$ (ref. [8]) or $[(Ar^*Ga)_2(CH)_2(CPh)_2]^{2-}$ with $Ar^* = C_6H_3$-2,6-$(C_6H_3$-2,6-$^i Pr_2)_2$ (ref. [9])), the formation of planar cycles that exhibit ring currents indicative of π-aromaticity has been reported for considerably fewer examples in purely inorganic systems. As shown in Fig. 1c, several aromatic molecules with up to 10 atoms have been experimentally realized that exhibit $4n+2$ π-aromaticity[10]. The smallest examples are borane derivatives based on B_3 and B_4 moieties with two π-electrons[11–14]. Most species exhibit six π-electrons: '$[(RSi)_4]^{2-}$' in $[\{\eta^4$-$(RSi)_4\}Ru(CO)_3]$ ($R = SiMe^tBu_2$)[15], the carbon-free rings S_2N_2 (ref. [16]), Ch_4^{2+} (Ch = S, Se, Te)[17,18] and Pn_4^{2-} (Pn = P, As (refs. [19,20]); note that Sb_4^{2-} and Bi_4^{2-} are weakly π-antiaromatic[21,22]) and the $(C_5H_5)^-$ and C_6H_6 analogues $P_2N_3^-$ (refs. [23]), Pn_5^- (Pn = P, As)[24] and Pn_6 (Pn = P, As)[24]. Larger S–N rings possess 10 π-electrons (S_4N_2, $S_3N_3^-$, $S_4N_3^+$, $S_4N_4^{2+}$) or 14 π-electrons ($S_4N_5^-$, $S_5N_5^+$)[16]. Some of these cycles show similarities to their organic analogues, for example as ligands in sandwich complexes like $[(Cp^*Mo)_2Pn_n]$ ($Cp^* = C_5Me_5$ or C_5Me_4Et; Pn = P, As; $n = 5, 6$)[24]. However, they usually exhibit lower stabilities, and their reactivities differ from the typical substitution chemistry of their organic cousins because of their varied electronic structures, all of which is of general interest for synthetic chemistry and the development of new compounds from such species.

The fewest examples are found in the family of all-metal π-aromatic compounds (Fig. 1d), with the ring size limited to five atoms and the number of π-electrons being two or six in all reported cases. It was first suggested in 1995 that a cyclic trigallane cluster anion, $[(RGa)_3]^{2-}$ ($R = C_6H_3$-2,6-$(C_6H_2$-2,4,6-$Me_3)_2)$[25,26], the Al analogue of which was reported 10 years later[27], behaves electronically like the isoelectronic cyclopropenyl cation $(C_3H_3)^+$ with two π-electrons. In 2001, the square planar 'Tr_4^{2-}' metal cycles in

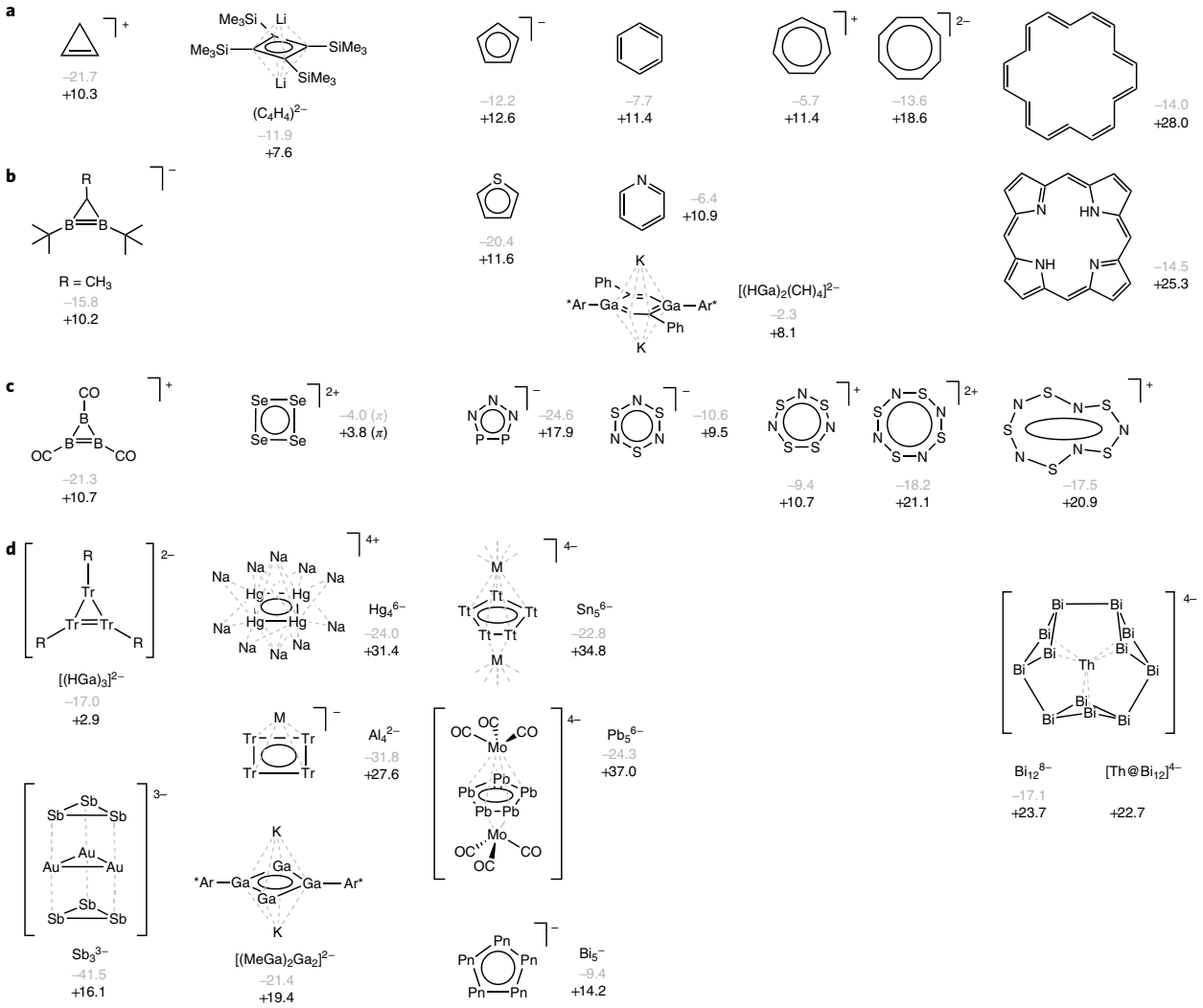

Fig. 1 | Survey of different classes of experimentally secured molecules exhibiting $4n+2$ π-aromaticity. NICS values (in ppm, grey) and ring currents (in nA T^{-1}, black) were calculated at the PBE/def2-TZVP/grid3 level of theory[48–53,59], with the conductor-like screening model (COSMO) applied for anions[54]. Simplifications of the molecules for the calculations are shown. From left to right: molecules with three to eight atoms and examples with more than eight atoms (rightmost) contributing to the $4n+2$ π-aromatic system. Missing entries indicate that no example has been reported for the respective class. **a**, Representatives of C–H aromatic molecules (with $Li_2[(Me_3SiC)_4]$ (ref. [7]) as a rare example of a four-membered cycle). **b**, Representatives of heteroaromatic molecules (with $K[(B^tBu)_2CCH(SiMe_3)_2]$ as a rare example of a three-membered cycle[8] and $[(Ar^*Ga)_2(CH_2)(CPh)_2]^{2-}$ as a representative of metallaaromatic molecules; $Ar^* = C_6H_3$-2,6-$(C_6H_3$-2,6-$^iPr_2)_2$; ref. [9]). **c**, Examples of purely inorganic, non-metal aromatic molecules (with the gas-phase species $[B_3(CO)_3]^+$ as a rare example of a three-membered cycle)[11]. **d**, Survey of all known types of molecules exhibiting all-metal π-aromaticity, with their stabilizing atoms or groups: Tr = Al, Ga and R = C_6H_3-2,6-$(C_6H_2$-2,4,6-$Me_3)_2$ in $[(RTr)_3]^{2-}$ (refs. [25–27]); M/Tr = Li/Al, Na/Al, Cu/Al, Na/In, Na/Ga in gas-phase species $[MTr_4]^-$ (refs. [28,29]); $Ar^* = C_6H_3$-2,6-$(C_6H_2$-2,4,6-$^iPr_3)_2$] in $[(Ar^*Ga)_2Ga_2]^{2-}$ (ref. [32]); Tt = Sn, Pb (ref. [36]); Pn = Sb, Bi in gas-phase species Pn_5^- (ref. [34]). NICS values and ring currents are given for one homologue only, as numbers within the homologous series are similar. Note that the numbers refer to total ring currents unless noted otherwise. This may include additional contributions of σ-aromaticity. Weakly π-antiaromatic Pn_4^{2-} (Pn = Sb, Bi)[21,22] are not listed here. For further references, see the text. Further details of the NICS and ring current calculations are provided in the Supplementary Information.

$[MTr_4]^-$ anions produced in gas-phase experiments (M/Tr = Li/Al, Na/Al, Cu/Al, Na/Ga, Na/In)[28,29] were classified as aromatic molecules with two completely delocalized π-electrons, which led to the introduction of the term 'all-metal aromaticity'[30]. The series of experimentally accessible species has expanded to include some further three-membered, four-membered and five-membered metal cycles: 'Sb_3^{3-}' (in $[(Sb_3)_2Au_3]^{3-}$)[31], '$[Ga_4]^{4-}$' (in $[(Ar^*Ga)_2Ga_2]^{2-}$; $Ar^* = C_6H_3$-2,6-$(C_6H_2$-2,4,6-$iPr_3)_2$)[32], Hg_4^{6-} (ref. [33]), Pn_5^- (Pn = Sb, Bi; gas phase only)[34] and Tt_5^{6-} (Tt = Sn, Pb)[35] with six π-electrons, as well as Pb_5^{2-} (in $[Pb_5\{Mo(CO)_3\}_2]^{4-}$)[36] with two π-electrons. Further cycles bearing π-aromaticity, like M_3^q (M/q = Zn/2−, Cd/2−, Hg/2−, Ta/1−, Hf/0)[37] or Mg_3^{2-} (ref. [38]), have been theoretically predicted, yet have not proved detectable so far in this form. It is worth noting that several other species were identified to show effective σ delocalization[39–42], which cannot easily be discriminated from the classical superatom model that is related to the Jellium model for spherical metal

clusters[43]. The relatively small number of species quoted above highlights the current limits of the all-metal π-aromatic systems experimentally secured so far. On the other hand, the ring currents shown in Fig. 1 indicate that these can indeed surmount those of organic systems, which suggests fundamentally different electronic and chemical properties are to be expected from such species. However, up to now, all isolable all-metal aromatic rings have been stabilized from 'outside'—by incorporation into a neat intermetallic solid or by attachment of protective organic groups, metal ions or transition metal complex fragments. This largely reduces the accessibility of the cycles, and thus the possibility of studying reactions involving the aromatic ring.

An approach for the formation of accessible all-metal aromatic molecules would be the stabilization of distinctly larger cycles from 'inside', which previously allowed the formation of spherical intermetalloid clusters only[44]. Very recently, Sun and others synthesized lanthanide ion-centred polystibide clusters of the type $[Ln@Sb_{12}]^{3-}$ (Ln = La, Y, Ho, Er, Lu), which were described as a combination of three π-antiaromatic Sb_4^{2-} moieties that are connected to form an 'Sb_{12}^{6-}' belt embedding an Ln^{3+} ion[45]. At the same time, we presented the topologically related, yet more highly charged, polybismuthide substructure in $[U@Bi_{12}]^{3-}$ (ref. [46]). An inspection of the aromaticity in this system was inhibited by the open-shell situation (due to an unpaired *f* electron), but the highest occupied molecular orbital (HOMO) suggested inherent π-electron delocalization.

Hence, our straightforward idea of how to (1) generate and (2) verify an all-metal π-aromatic cluster was to replace U with an earlier actinide that would not bear an unpaired electron, while still allowing the high charge to remain on the ring. This approach was explored successfully by using Th^{4+} as the central ion, with no pronounced tendency of withdrawing electrons from the polymetallide ring due to the high stability of the +4 oxidation state of thorium. Here, we present the synthesis and crystal structure of $[K(crypt\text{-}222)]_4[Th@Bi_{12}]\cdot 2en$ (where en is ethane-1,2-diamine), comprising the anionic cluster $[Th@Bi_{12}]^{4-}$. Magnetic measurements and quantum chemical studies confirm the formal assignment as Th^{4+} and 'Bi_{12}^{8-}'. Structural features and calculated ring currents as well as NICS values indicate the latter to be aromatic, with two π-electrons causing a remarkably strong ring current that is similar to the one in porphine (26π), despite a much smaller number of π-electrons to be delocalized over the uncommon polymetallide architecture. This anion is an all-metal π-aromatic molecule that exists without additional (external) coordination in the crystal and in solution. It even survives the transfer into the gas phase in the given composition under mass spectrometry conditions.

Results and discussion

Synthesis and structure of $[K(crypt\text{-}222)]_4[Th@Bi_{12}]\cdot 2en$ (2). The reaction of $[ThCp^{\#}{}_3Cl]$ (**1**; $Cp^{\#} = C_5Me_4H$) with $K_5Ga_2Bi_4$ (**A**), as an in situ source of $(GaBi_3)^{2-}$ and Bi_4^{2-} (refs. [21,47]) was performed in ethane-1,2-diamine (en) in the presence of the cation sequestration agent 4,7,13,16,21,24-hexaoxa-1,10-diazabicyclo[8.8.8] hexacosane (crypt-222). Following filtration, layering of the filtrate with toluene and storage at 5 °C, the formation of black, prismatic crystals was obtained after 10 days (for further details of the synthesis, see Methods). Using single-crystal X-ray diffraction (Supplementary Table 1), the composition of the crystals was determined to be $[K(crypt\text{-}222)]_4[Th@Bi_{12}]\cdot 2en$ (**2**), and the Th:Bi ratio of **2** was verified by micro-X-ray fluorescence spectroscopy (μ-XFS; Supplementary Fig. 6 and Supplementary Table 2). Compound **2** comprises the novel Th-centred intermetalloid cluster anion $[Th@Bi_{12}]^{4-}$ (**2A**), the composition of which was additionally confirmed by electrospray ionization mass spectrometry (ESI-MS; Supplementary Fig. 9). The molecular structure of **2A** is illustrated in Fig. 2.

According to single-crystal X-ray structure analysis, cluster **2A** adopts the same overall architecture as $[U@Bi_{12}]^{3-}$. Three four-membered, folded $\{Bi_4\}$ rings are connected at opposing corners to create a doughnut-shaped $\{Bi_{12}\}$ ring enclosing the actinide ion in its centre. Two different types of Bi–Bi bond are observed, with those between the four-membered rings (d_A) being slightly shorter, on average, than those within the rings (d_B). This is like the situation in $[U@Bi_{12}]^{3-}$, but it is in striking contrast to the structural properties of the $[Ln@Sb_{12}]^{3-}$ series mentioned above. As discussed in the following, this structural detail informs us about the frontier orbital situation (and hence the situation near the energy level of the highest and lowest molecular orbitals, HOMO and LUMO), and as such provides a strong indication of the successful generation of an all-metal π-aromatic cluster in **2A**. This can be qualitatively connected to the symmetry criterion for aromatic molecules: first, the $\{Bi_{12}\}$ subunit exhibits an overall much narrower range of bond lengths in **2A** (Bi–Bi 3.0420(14)–3.132(1) Å) as compared to the range reported for the $\{Sb_{12}\}$ subunit in $[La@Sb_{12}]^{3-}$ (2.8088(5)–3.0517(5) Å). Second, the relatively small Bi_A–Bi_A' distances (3.0420(14)–3.0785(13) Å) indicate a strengthening of the respective bonds and the presence of π interactions in **2A**, as compared to the relatively large Sb–Sb distances between the corresponding $\{Sb_4\}$ units in $[La@Sb_{12}]^{3-}$ (3.0179(6)–3.0517(5) Å). Although it is difficult to comment on the relative stability of the aromatic molecule (as a third criterion), because no related system is known so far for the given elemental composition, it is notable that anion **2A** exhibits a considerable (thermal) stability both in the condensed phase (crystal and solution) and even in the gas phase (cf. the mass spectra), without the presence of externally stabilizing ligands or additional cations. It might therefore be a good candidate to eventually study the reactivity of all-metal π-aromatic molecules in solution for the first time.

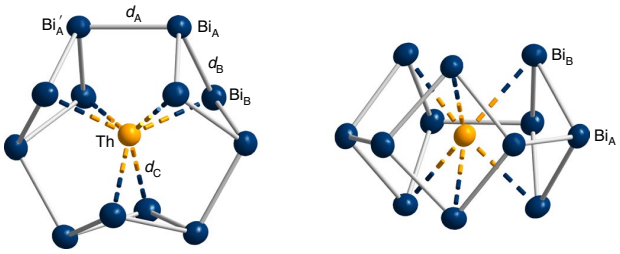

Fig. 2 | Molecular structure of the cluster anion $[Th@Bi_{12}]^{4-}$ in compound 2. The molecule is shown in two different orientations with displacement ellipsoids drawn at the 50% probability level at 100(2) K. Ranges of selected distances (in Å): Bi_A–$Bi_A' = d_A$ 3.0420(14)–3.0785(13), Bi_A–$Bi_B = d_B$ 3.0440(11)–3.132(1), Th–$Bi_B = d_C$ 3.2104(11)–3.2571(9), Th–Bi_A 3.5251(13)–3.5908(9).

Quantum chemical study of the geometric and electronic structure of $[Th@Bi_{12}]^{4-}$ (2A). To verify the success of our concept, density functional theory (DFT) calculations were carried out with the program system TURBOMOLE[48,49], using the PBE functional (developed by Perdew, Burke, and Ernzerhof)[50]. For Th, an effective core potential covering the 78 inner electrons (ECP-78)[51] was employed together with a triple-zeta basis[51], and for Bi an ECP-60[52] with a triple-zeta basis[53]. The negative charge was compensated by employing the conductor-like screening model (COSMO) with default parameters[54]. The geometric structure of **2A** is well reproduced by the calculated distances (deviations amount to ~0.01 Å). In particular, as in the experiment, d_A is shorter than d_B by 0.03 Å, like in $[U@Bi_{12}]^{3-}$. Note that the inverse trend applies for the hypothetical '$[La@Bi_{12}]^{3-}$', which behaves like the experimentally determined $[La@Sb_{12}]^{3-}$ mentioned above.

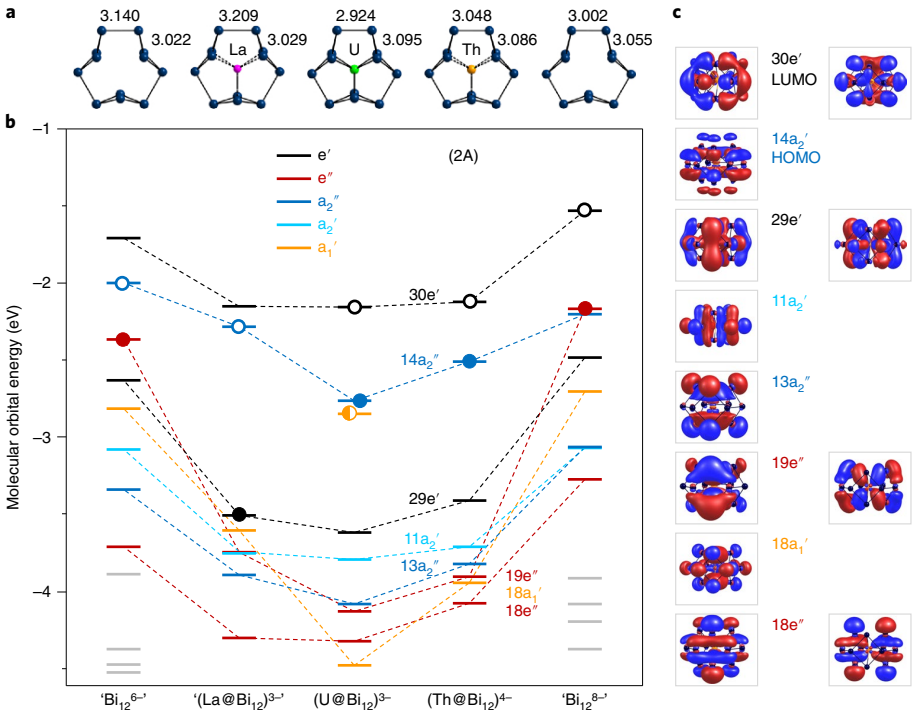

Fig. 3 | Frontier orbital region of the molecular orbital schemes of anions based on 12-atomic polybismuthide rings. a, Structure images of the calculated molecules (D_{3h} symmetry; Bi–Bi distances in Å). Atomic coordinates and contributions to all valence molecular orbitals are given in a separate file as part of the Supplementary Information and in Supplementary Tables 8–12, respectively. **b**, Frontier orbitals of the respective molecules: different irreducible representations are shown in different colours for clarity (molecular orbital levels drawn in grey are those that lie within the chosen energy range for the empty polybismuthide cycles only). The dashed lines serve as a guide to the eye to denote changes in the corresponding molecular-orbital energies. The energy of the HOMO is indicated by a filled circle and the lowest unoccupied molecular orbital (LUMO) by an open circle for each species; the singly occupied *f* orbital (HOMO-1, a_1') of $[U@Bi_{12}]^{4-}$ is indicated by a half-filled circle. **c**, Illustration of molecular orbitals of $[Th@Bi_{12}]^{4-}$ (**2A**) in side view, with contours drawn at isovalues of ±0.02 a.u. in blue and red. Contributions from atomic orbitals to all valence molecular orbitals are provided in Supplementary Tables 8–12.

To place the electronic situation in **2A** in the context of related (hypothetical or known) anions based on 12-atomic polybismuthide rings, we also calculated 'Bi_{12}^{6-}', '$[La@Bi_{12}]^{3-}$', $[U@Bi_{12}]^{3-}$, and 'Bi_{12}^{8-}'. Figure 3a presents the calculated molecular structures of these species and **2A**, while the frontier orbital regions of their molecular orbitals are given in Fig. 3b (the complete set of valence molecular orbitals is provided in Supplementary Fig. 16), with the respective molecular orbitals of **2A** illustrated in Fig. 3c.

Owing to the different total electron counts, 66 in 'Bi_{12}^{6-}' and '$[La@Bi_{12}]^{3-}$', 69 in $[U@Bi_{12}]^{3-}$, and 68 in **2A** and 'Bi_{12}^{8-}', the molecular orbital denoted as the irreducible representation $14a_2''$ in **2A** is the LUMO in '$[La@Bi_{12}]^{3-}$', while it is the HOMO in $[U@Bi_{12}]^{3-}$ and **2A**. The occupation of this a_2'' molecular orbital is directly correlated with d_A being shorter than d_B, as this orbital is bonding in d_A but anti-bonding in d_B. As is evident from Fig. 3b, the most obvious difference in the electronic structures of $[Th@Bi_{12}]^{4-}$ (**2A**) and $[U@Bi_{12}]^{3-}$ is one unpaired electron residing in the HOMO-1 (a_1') of $[U@Bi_{12}]^{3-}$, leading to a doublet state, while **2A** represents the desired closed-shell case. In contrast to $[U@Bi_{12}]^{3-}$, none of the molecular orbitals in $[Th@Bi_{12}]^{4-}$ shows any notable 5*f* contribution (results of a Mulliken population analysis are shown in Fig. 3c and Supplementary Table 11)[55]. This is in perfect agreement with the measurement of the magnetic susceptibility, which reveals the diamagnetic nature of compound **2** (Supplementary Fig. 12). Overall, the situation in **2A** is indeed described best as Th^{4+} residing in a cyclic Bi_{12}^{8-} unit.

A comparison of the frontier orbitals of all five species, 'Bi_{12}^{6-}', '$[La@Bi_{12}]^{3-}$', $[U@Bi_{12}]^{3-}$, $[Th@Bi_{12}]^{4-}$ (**2A**), and 'Bi_{12}^{8-}', indicates the following major characteristics: the central ion strongly influences the molecular-orbital energy levels with regard to the empty $\{Bi_{12}\}$ rings, mostly as a consequence of electrostatic interactions. Somewhat larger stabilizations are found for the molecular orbitals that are denoted as $18a_1'$ and $19e''$ in **2A**, which exhibit some *d*-orbital contribution of the inner metal atom (for example, 0.33 e^- and 0.69 e^- for **2A**, according to the Mulliken analysis; Supplementary Tables 8–12). The most important feature regarding aromaticity, however, is the occupation or non-occupation of the molecular orbital denoted as $14a_2''$ in **2A**, as discussed in the following.

Quantum chemical investigation of the *π*-aromaticity in $[Th@Bi_{12}]^{4-}$ (2A). As already known, *π*-aromatic compounds gain stability by inherent delocalization of $4n+2$ *π*-electrons over the ring system. To probe whether **2A** exhibits this kind of delocalization, as suggested by the shape of the HOMO ($14a_2''$, Fig. 4a), we carried out a localization procedure for the 34 valence molecular orbitals using the Boys method[56] (Fig. 4b–g) and further calculated the intrinsic bond orbitals (IBOs; Supplementary Fig. 13)[57]. From both procedures, we obtained 33 localized orbitals representing either two-centre bonds (nonpolar Bi–Bi bonds, Fig. 4c,d) slightly polarized towards Th and strongly polar Th–Bi bonds (Fig. 4e) or lone pairs (one per Bi atom, Fig. 4f,g). One orbital is remaining,

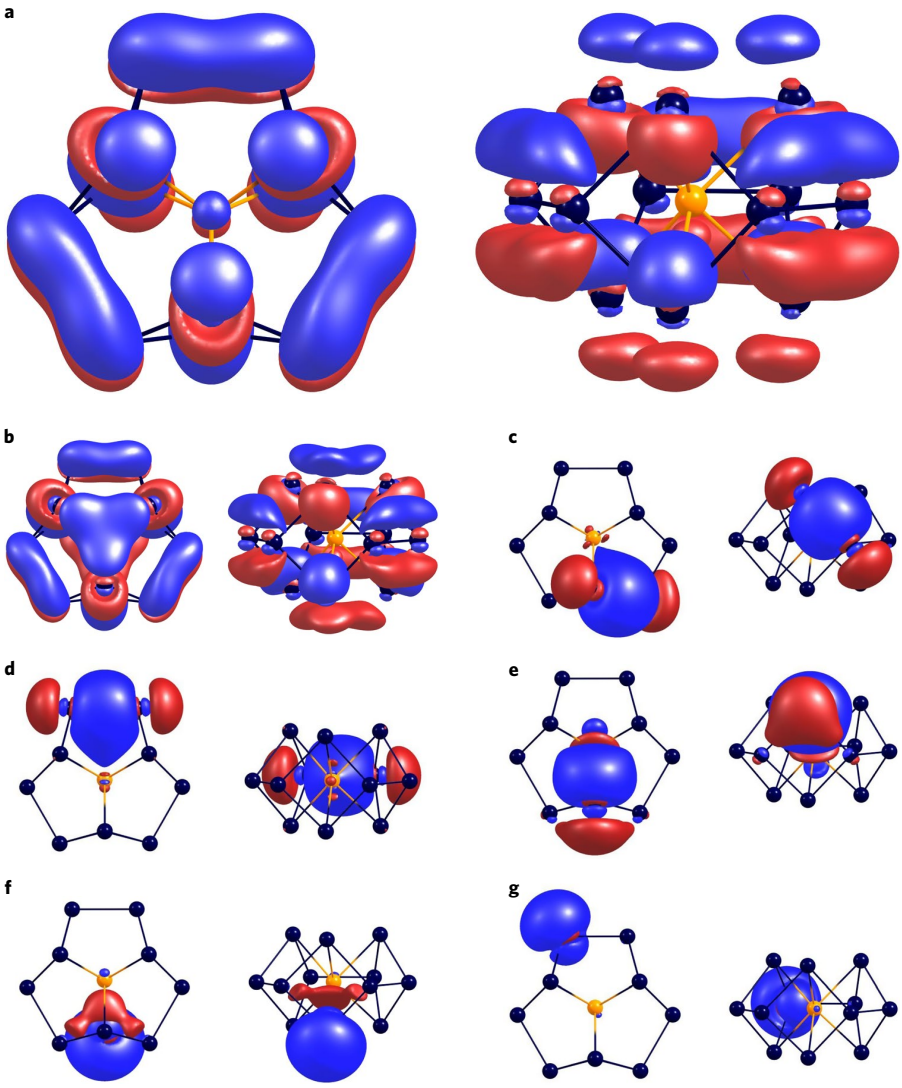

Fig. 4 | HOMO of the cluster anion $[Th@Bi_{12}]^{4-}$ and localized molecular orbitals (LMOs) from a Boys localization procedure in top and side views. **a**, The HOMO (character a_2'' in D_{3h} symmetry). **b**, The LMO with the highest energy expectation value shows contributions from all 12 Bi atoms and has almost the same shape as the HOMO, which indicates intrinsic electron delocalization. **c**, Two-centre LMO representing a Bi–Bi bond within a Bi_4 ring. **d**, Two-centre LMO representing a Bi–Bi bond between two Bi_4 rings. **e**, Two-centre LMO representing a Bi–Th bond. **f**, One-centre LMO representing a lone pair at a Bi atom above/below the equatorial plane of the molecule. **g**, One-centre LMO representing a lone pair at a Bi atom within the equatorial plane of the molecule. Contours are drawn at isovalues of ±0.02 a.u. in blue and red, for approximately the same orientation of the molecule as shown in Fig. 2.

however, which is delocalized over the entire cycle with contributions from all 12 Bi atoms. This orbital, shown in Fig. 4b, and the canonical HOMO, shown in Fig. 4a, exhibit essentially the same shape, which clearly shows the intrinsic delocalization of two electrons in **2A**. This is corroborated by a comparison of the electron localization function (ELF)[58] calculated for the two $\{Bi_{12}\}$ cycles 'Bi_{12}^{6-}' and 'Bi_{12}^{8-}' (Supplementary Fig. 14), indicating the π delocalization of the respective two electrons in the 12-membered ring.

All experimental and quantum chemical findings described so far are strong indications for a π-aromatic situation within this cyclic polybismuthide. Thus, we calculated the magnetically induced current density to study the aromaticity based on the magnetic criterion[2–5] and the electron delocalization pathways of the cluster. This was done with the gauge-including magnetically induced currents (GIMIC) method[59]. A plot of the magnetically induced current density is provided in Fig. 5. The torus-shaped current density is similar to that in planar rings, despite the perpendicularly oriented Bi_B atoms (Fig. 2). Hence, the π-aromatic system is indeed best described as a cycle (or a 'belt'). By numerical integration along a plane perpendicular to the Bi_A–Bi_A' bond and parallel to the magnetic field direction, a diatropic net ring current of 22.7 nA T^{-1} was found. When using more sophisticated scalar-relativistic all-electron approaches (X2C)[60–63], the value is even increased to 24.8 nA T^{-1}. These values are roughly twice the ring current of 6π-aromatic benzene (11.4 nA T^{-1}) and close to that of 26π-aromatic porphine, which is often simplified to an 18π-aromatic compound (25.3 nA T^{-1})[64]. Therefore, $[Th@Bi_{12}]^{4-}$ is clearly proven to be π-aromatic based on the structural and magnetic criteria.

Notably, the (hypothetical) 'Bi_{12}^{8-}' ring alone shows essentially the same level of aromaticity (23.7 nA T^{-1}; Supplementary

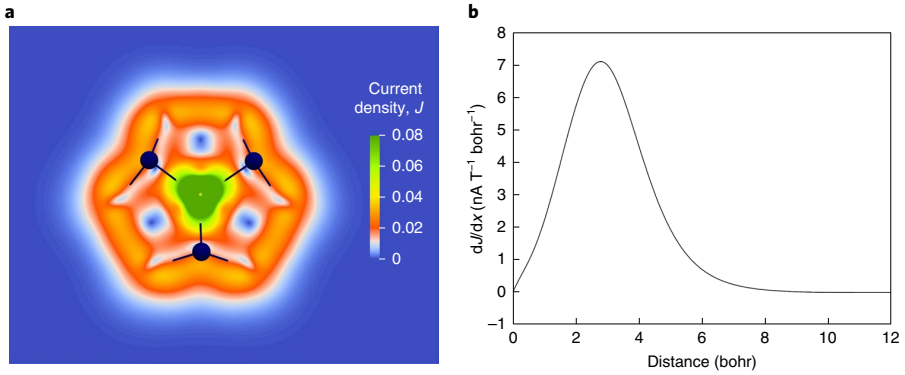

Fig. 5 | Calculated ring currents in $[Th@Bi_{12}]^{4-}$. a, Plot of the magnetically induced current density (in atomic units), 2 bohr above the molecular plane of $[Th@Bi_{12}]^{4-}$. The magnetic field is perpendicular to the molecular plane. **b**, Profile of the magnetically induced current density to determine the boundaries for the numerical integration. The origin is at the zero point of the induced current density between the Bi_A–$Bi_{A'}$ bond and the Th atom (see Supplementary Information for details).

Information). So, the Th^{4+} ion is indeed mainly required to enable its synthetic access by stabilizing the cycle. Another frequently used quantity for the quantum chemical indication of aromaticity is NICS[6], which indirectly probes the magnetically induced current density. This method also suggests aromaticity because of NICS values of approximately −17 ppm (ECPs) and −16 ppm (X2C) for the hypothetical 'Bi_{12}^{8-}' (Supplementary Table 4). For comparison, the ring currents and NICS values of Al_4^{2-} are 27.6 nA T^{-1} and −31.8 ppm, respectively (Fig. 1). Although the two π-electrons are delocalized over four atoms in 'Al_4^{2-}', the delocalization involves 12 atoms in **2A**, without a drop in the ring current strength.

Finally, to probe the applicability of the $4n+2$ π rule to this class of compounds, we also studied the next (hypothetical) cousins in this series, 'Bi_{12}^{10-}' and 'Bi_{12}^{12-}', with four or six π-electrons, respectively. Although 'Bi_{12}^{10-}' possesses a triplet ground state (like the famous antiaromatic square planar cyclobutadiene), we calculate a ring current of 42.9 nA T^{-1} and a NICS value of −34 ppm for 'Bi_{12}^{12-}', indicating notable π-aromaticity. However, it is unlikely that a polybismuthide of this charge could be synthesized from solution.

To summarize, we have presented the targeted synthesis of $[K(crypt\text{-}222)]_4[Th@Bi_{12}]\cdot 2en$ (**2**) with a $[Th@Bi_{12}]^{4-}$ anion (**2A**), which is best described as a highly symmetric 'Bi_{12}^{8-}' ring embedding a central Th^{4+} ion. The entire anion can be transferred into solution, and it stays intact under ESI-MS conditions, indicating considerable thermodynamic stability. The HOMO of the anion shows π delocalization and, in contrast to all other molecular orbitals, it is inherently not localizable. This renders **2A**, in particular the $\{Bi_{12}\}$ moiety in it, a new type of a $4n+2$ π-aromatic system (with $n=0$), which is based on an uncommon cyclic molecular structure that is neither planar nor spherical. Quantum chemical studies further indicate a remarkable ring current strength of 24.8 nA T^{-1} for $[Th@Bi_{12}]^{4-}$ (and 23.7 nA T^{-1} for 'Bi_{12}^{8-}'), which is much larger than in 6π-aromatic benzene (11.4 nA T^{-1}). It is indeed similar to that in 26π-aromatic porphine (25.3 nA T^{-1}), in spite of the notably lower number of π-electrons involved, and to that in 'Al_4^{2-}' (27.6 nA T^{-1}), in spite of the much larger number of metal atoms involved. The central Th^{4+} ion mainly serves to help the formation of the cycle and to stabilize it 'from inside', like a very uncommon type of metal complex with an aromatic ligand. This way, the molecule is generally accessible for post-synthetic chemistry in the condensed phase, which is unprecedented in the field of all-metal π-aromaticity.

The formation and isolation of compound **2** has hence opened a new chapter in this field, which may be expanded in future work by extension to other main group metals and other highly charged inner metal ions to fine-tune the electronic properties. We hope that our findings will help towards the targeted construction of even more complex heavy-metal cycles displaying all-metal π-aromaticity, and in turn new prospects for cluster-based chemistry.

References

1. Hückel, E. Quantentheoretische Beiträge zum Benzolproblem. I. Die Elektronenkonfiguration des Benzols und verwandter Beziehungen. *Z. Phys.* **70**, 204–286 (1931).
2. McNaught, A. D. & Wilkinson, A. *IUPAC. Compendium of Chemical Terminology* 2nd edn (Blackwell Scientific Publications, 1997); online version (2019) created by S. J. Chalk.
3. Schleyer, P. V. R. & Jiao, H. What is aromaticity? *Pure Appl. Chem.* **68**, 209–221 (1996).
4. Gershoni-Poranne, R. & Stanger, A. Magnetic criteria of aromaticity. *Chem. Soc. Rev.* **44**, 6597–6615 (2015).
5. Sundholm, D., Fliegl, H. & Berger, R. J. Calculation of magnetically induced current densities: theory and applications. *Wiley Interdiscip. Rev. Comput. Mol. Sci.* **6**, 639–678 (2016).
6. Schleyer, P. V. R., Maerker, C., Dransfeld, A., Jiao, H. & Hommes, N. Nucleus-independent chemical shifts: a simple and efficient aromaticity probe. *J. Am. Chem. Soc.* **118**, 6317–6318 (1996).
7. Sekiguchi, A., Matsuo, T. & Watanabe, H. Synthesis and characterization of a cyclobutadiene dianion dilithium salt: evidence for aromaticity. *J. Am. Chem. Soc.* **122**, 5652–5653 (2000).
8. Wehrmann, R., Meyer, H. & Berndt, A. Diboriranides and a 1,3-diboraallyl system with B-H-B bridge. *Angew. Chem. Int. Ed.* **24**, 788–790 (1985).
9. Zhu, Z., Wang, X., Olmstead, M. M. & Power, P. P. Synthesis and characterization of $[Ar'GaC(Ph)CH]_2$ and $K_2[Ar'GaC(Ph)CH]_2\cdot OEt_2$: from digallene to digallacyclohexadiene to digallatabenzene. *Angew. Chem. Int. Ed.* **48**, 2027–2030 (2009).
10. De Proft, F. et al. Ring currents as probes of the aromaticity of inorganic monocycles: P_5^-, As_5^-, S_2N_2, $S_3N_3^-$, $S_4N_3^+$, $S_4N_4^{2+}$, $S_5N_5^+$, S_4^{2+} and Se_4^{2+}. *Chem. Eur. J.* **10**, 940–950 (2004).
11. Jin, J. et al. The $[B_3(NN)_3]^+$ and $[B_3(CO)_3]^+$ complexes featuring the smallest π-aromatic species B_3^+. *Angew. Chem. Int. Ed.* **55**, 2078–2082 (2016).
12. Unverzagt, M. et al. Carbene analogues of boron stabilized by neighboring B–B moieties: doubly aromatic bishomotriboriranides. *Angew. Chem. Int. Ed.* **36**, 1469–1472 (1997).

13. Präsang, C., Hofmann, M., Geiseler, G., Massa, W. & Berndt, A. Aromatic boranes with planar-tetracoordinate boron atoms and very short B–B distances. *Angew. Chem. Int. Ed.* **41**, 1526–1529 (2002).
14. Maier, A., Hofmann, M., Pritzkow, H. & Siebert, W. A planar, aromatic bicyclo-tetraborane(4). *Angew. Chem. Int. Ed.* **41**, 1529–1532 (2002).
15. Takanashi, K., Lee, V. Y. & Sekiguchi, A. Tetrasilacyclobutadiene and cyclobutadiene tricarbonylruthenium complexes: η^4-(^{t}Bu$_2$MeSi)$_4$Si$_4$]Ru(CO)$_3$ and [η^4-(Me$_3$Si)$_4$C$_4$]Ru(CO)$_3$. *Organometallics* **28**, 1248–1251 (2009).
16. Gleiter, R. Structure and bonding in cyclic sulfur–nitrogen compounds—molecular orbital considerations. *Angew. Chem. Int. Ed.* **20**, 444–452 (1981).
17. Bucholz, C. F. Versuche über die Auflösung des Indigs in der Schwefelsäure, als Beytrag zur Ausmittelung des Vorgangs bey Verselben. *Gehlen's Neues J. Chem.* **3**, 3–29 (1804).
18. Gillespie, R. J. & Passmore, J. Polycations of group VI. *Acc. Chem. Res.* **4**, 413–419 (1971).
19. Kraus, F., Aschenbrenner, J. C. & Korber, N. P_4^{2-}: a 6π aromatic polyphosphide in dicesium cyclotetraphosphide–ammonia (1/2). *Angew. Chem. Int. Ed.* **42**, 4030–4033 (2003).
20. Korber, N. & Reil, M. An isolated cyclo-tetraarsendiide: low temperature synthesis and crystal structure of bis-pentaamminesodium tetraarsendiide–ammonia (1/3) [Na(NH$_3$)$_5$]$_2$As$_4$·3NH$_3$. *Chem. Commun.* 84–85 (2002); https://doi.org/10.1039/b108879c
21. Cisar, A. & Corbett, J. D. Polybismuth anions. Synthesis and crystal structure of a salt of the tetrabismuthide(2−) ion, Bi_4^{2-}. A basis for the interpretation of the structure of some complex intermetallic phases. *Inorg. Chem.* **16**, 2482–2487 (1977).
22. Critchlow, S. C. & Corbett, J. D. Homopolyatomic anions of the post transition elements. Synthesis and structure of potassium-crypt salts of the tetraantimonide(2−) and heptaantimonide(3−) anions, Sb_4^{2-} and Sb_7^{3-}. *Inorg. Chem.* **23**, 770–774 (1984).
23. Velian, A. & Cummins, C. C. Synthesis and characterization of $P_2N_3^-$: an aromatic ion composed of phosphorus and nitrogen. *Science* **348**, 1001–1004 (2015).
24. Scherer, O. J. Complexes with substituent-free acyclic and cyclic phosphorus, arsenic, antimony and bismuth ligands. *Angew. Chem. Int. Ed.* **29**, 1104–1122 (1990).
25. Li, X.-W., Pennington, W. T. & Robinson, G. H. A metallic system with aromatic character. Synthesis and molecular structure of Na$_2$[(Mes$_2$C$_6$H$_3$)Ga]$_3$ (Mes = 2,4,6-Me$_3$C$_6$H$_2$): the first cyclogallane. *J. Am. Chem. Soc.* **117**, 7578–7579 (1995).
26. Li, X.-W. et al. Cyclogallanes and metalloaromaticity. Synthesis and molecular structure of dipotassium tris((2,6-dimesitylphenyl)cyclogallene), K$_2$[(Mes$_2$C$_6$H$_3$)Ga]$_3$ (Mes = 2,4,6-Me$_3$C$_6$H$_2$): a structural and theoretical examination. *Organometallics* **15**, 3798–3803 (1996).
27. Wright, R. J., Brynda, M. & Power, P. P. Synthesis and structure of the 'dialuminyne' Na$_2$[Ar′AlAlAr′] and Na$_2$[(Ar″Al)$_3$]: Al—Al bonding in Al_2Na_2 and Al_3Na_2 clusters. *Angew. Chem. Int. Ed.* **45**, 5953–5956 (2006).
28. Li, X. L., Kuznetsov, A. E., Zhang, H.-F., Boldyrev, A. I. & Wang, L.-S. Observation of all-metal aromatic molecules. *Science* **291**, 859–861 (2001).
29. Kuznetsov, A. E., Boldyrev, A. I., Li, X. & Wang, L.-S. On the aromaticity of square planar Ga_4^{2-} and In_4^{2-} in gaseous $NaGa_4^-$ and $NaIn_4^-$ clusters. *J. Am. Chem. Soc.* **123**, 8825–8831 (2001).
30. Boldyrev, A. I. & Wang, L. S. All-metal aromaticity and antiaromaticity. *Chem. Rev.* **105**, 3716–3757 (2005).
31. Pan, F.-X. et al. An all-metal aromatic sandwich complex $[Sb_3Au_3Sb_3]^{3-}$. *J. Am. Chem. Soc.* **137**, 10954–10957 (2015).
32. Twamley, B. & Power, P. P. Synthesis of the square-planar gallium species K$_2$[Ga$_4$(C$_6$H$_3$-2,6-Trip$_2$)$_2$] (Trip = C$_6$H$_2$-2,4,6-^{i}Pr$_3$): the role of aryl–alkali metal ion interactions in the structure of gallium clusters. *Angew. Chem. Int. Ed.* **39**, 3500–3503 (2000).
33. Kuznetsov, A. E., Corbett, J. D., Wang, L. S. & Boldyrev, A. I. Aromatic mercury clusters in ancient amalgams. *Angew. Chem. Int. Ed.* **40**, 3369–3372 (2001).
34. Gausa, M., Kaschner, R., Lutz, H. O., Seifert, G. & Meiwes-Broer, K.-H. Photoelectron and theoretical investigations on bismuth and antimony pentamer anions: evidence for aromatic structure. *Chem. Phys. Lett.* **230**, 99–102 (1994).
35. Todorov, I. & Sevov, S. C. Heavy-metal aromatic rings: cyclopentadienyl anion analogues Sn_5^{6-} and Pb_5^{6-} in the Zintl phases Na_8BaPb_6, Na_8BaSn_6 and Na_8EuSn_6. *Inorg. Chem.* **43**, 6490–6494 (2004).
36. Yong, L., Hoffmann, S. D., Fässler, T. F., Riedel, S. & Kaupp, M. [Pb$_5${Mo(CO)$_3$}$_2$]$^{4-}$: a complex containing a planar Pb_5 unit. *Angew. Chem. Int. Ed.* **44**, 2092–2096 (2005).
37. Zubarev, D. Y., Averkiev, B. B., Zhai, H.-J., Wang, L.-S. & Boldyrev, A. I. Aromaticity and antiaromaticity in transition-metal systems. *Phys. Chem. Chem. Phys.* **10**, 257–267 (2008).
38. Kuznetsov, A. E. & Boldyrev, A. I. A single π-bond captures 3, 4 and 5 atoms. *Chem. Phys. Lett.* **388**, 452–456 (2004).
39. Liu, C., Popov, I. A., Chen, Z., Boldyrev, A. I. & Sun, Z.-M. Aromaticity and antiaromaticity in Zintl clusters. *Chem. Eur. J.* **24**, 14583–14597 (2018).
40. Huang, X., Zhai, H. -J., Kiran, B. & Wang, L. -S. Observation of *d*-orbital aromaticity. *Angew. Chem. Int. Ed.* **44**, 7251–7254 (2005).
41. Popov, I. A. et al. Peculiar all-metal σ-aromaticity of the $[Au_2Sb_{16}]^{4-}$ anion in the solid. *Angew. Chem. Int. Ed.* **55**, 15344–15346 (2016).
42. Liu, C. et al. $[Co_2@Ge_{16}]^{4-}$: localized versus delocalized bonding in two isomeric intermetalloid clusters. *Chem. Eur. J.* **24**, 699–705 (2018).
43. Jones, C. E. Jr. et al. Al_nBi clusters: transitions between aromatic and jellium stability. *J. Phys. Chem.* **112**, 13316–13325 (2008).
44. Wilson, R. J., Lichtenberger, N., Weinert, B. & Dehnen, S. Intermetalloid and heterometallic clusters combining p-block (semi)metals with d- or f-block metals. *Chem. Rev.* **119**, 8506–8554 (2019).
45. Min, X. et al. All-metal antiaromaticity in Sb_4-type lanthanocene anions. *Angew. Chem. Int. Ed.* **55**, 5531–5535 (2016).
46. Lichtenberger, N. et al. Main group metal–actinide magnetic coupling and structural response upon U^{4+} inclusion into Bi, Tl/Bi or Pb/Bi cages. *J. Am. Chem. Soc.* **138**, 9033–9036 (2016).
47. Xu, L. & Sevov, S. C. Heteroatomic deltahedral clusters of main-group elements: synthesis and structure of the Zintl ions $[In_4Bi_5]^{3-}$, $[InBi_3]^{2-}$ and $[GaBi_3]^{2-}$. *Inorg. Chem.* **39**, 5383–5389 (2000).
48. Turbomole version 7.4.1 2019 and version 7.5 2020 (University of Karlsruhe and Forschungszentrum Karlsruhe GmbH, 1989–2007, TURBOMOLE GmbH since 2007); https://www.turbomole.org
49. Balasubramani, S. G. et al. TURBOMOLE: modular program suite for ab initio quantum-chemical and condensed-matter simulations. *J. Chem. Phys.* **152**, 184107 (2020).
50. Perdew, J. P., Burke, K. & Ernzerhof, M. Generalized gradient approximation made simple. *Phys. Rev. Lett.* **77**, 3865–3868 (1996); erratum **78**, 1396 (1997).
51. Cao, X., Dolg, M. & Stoll, H. Valence basis sets for relativistic energy consistent small-core actinide pseudopotentials. *J. Chem. Phys.* **118**, 487–496 (2003).
52. Metz, B., Stoll, H. & Dolg, M. Small-core multiconfiguration-Dirac–Hartree–Fock-adjusted pseudopotentials for post-d main group elements: application to PbH and PbO. *J. Chem. Phys.* **113**, 2563–2569 (2000).
53. Weigend, F. & Ahlrichs, R. Balanced basis sets of split valence, triple zeta valence and quadruple zeta valence quality for H to Rn: design and assessment of accuracy. *Phys. Chem. Chem. Phys.* **7**, 3297–3305 (2005).
54. Schäfer, A., Klamt, A., Sattel, D., Lohrenz, J. C. W. & Eckert, F. COSMO Implementation in TURBOMOLE: extension of an efficient quantum chemical code towards liquid systems. *Phys. Chem. Chem. Phys.* **2**, 2187–2193 (2000).
55. Mulliken, R. S. Electronic population analysis on LCAO–MO molecular wave functions. I. *J. Chem. Phys.* **23**, 1833–1840 (1955).
56. Boys, S. F. Construction of some molecular orbitals to be approximately invariant for changes from one molecule to another. *Rev. Mod. Phys.* **32**, 296–299 (1960).
57. Knizia, G. Intrinsic atomic orbitals: an unbiased bridge between quantum theory and chemical concepts. *J. Chem. Theory Comput.* **9**, 4834–4843 (2013).
58. Becke, A. D. & Edgecombe, K. E. A simple measure of electron localization in atomic and molecular systems. *J. Chem. Phys.* **92**, 5397–5403 (1990).
59. Jusélius, J., Sundholm, D. & Gauss, J. Calculation of current densities using gauge-including atomic orbitals. *J. Chem. Phys.* **121**, 3952–3963 (2004); https://github.com/qmcurrents/gimic
60. Peng, D., Middendorf, N., Weigend, F. & Reiher, M. An efficient implementation of two-component relativistic exact-decoupling methods for large molecules. *J. Chem. Phys.* **138**, 184105 (2013).
61. Franzke, Y. J., Middendorf, N. & Weigend, F. Efficient implementation of one- and two-component analytical energy gradients in exact two-component theory. *J. Chem. Phys.* **148**, 104110 (2018).
62. Franzke, Y. J. & Weigend, F. NMR shielding tensors and chemical shifts in scalar-relativistic local exact two-component theory. *J. Chem. Theory Comput.* **15**, 1028–1043 (2019).
63. Franzke, Y. J., Treß, R., Pazdera, T. M. & Weigend, F. Error-consistent segmented contracted all-electron relativistic basis sets of double- and triple-zeta quality for NMR shielding constants. *Phys. Chem. Chem. Phys.* **21**, 16658–16664 (2019).
64. Franzke, Y. J., Sundholm, D. & Weigend, F. Calculations of current densities and aromatic pathways in cyclic porphyrin and isoporphyrin arrays. *Phys. Chem. Chem. Phys.* **19**, 12794–12803 (2017).

Methods

General methods. All manipulations and reactions were performed under a dry argon atmosphere using standard Schlenk or glovebox techniques with freshly dried and distilled solvents. Elements were used as received: K lumps, Acros Organics, 98%; Ga pellets, Alfa Aesar, 99,9999% (metals basis); Bi powder, ChemPur Karlsruhe, 99%. Ethane-1,2-diamine (en) and *N*,*N*-dimethylformamide (DMF; Aldrich, 99.8%) were distilled from CaH_2 and stored over 3-Å molecular sieves. Toluene (Acros Organics, 99%) was distilled from sodium-potassium alloy and stored over 4-Å molecular sieves. Kryptofix 222 (crypt-222, Merck) was dried under vacuum overnight. $K_5Ga_2Bi_4$ (**A**)[47], known as a source of $[K(crypt\text{-}222)]_2(GaBi_3)$ (**B**)[47] and $[K(crypt\text{-}222)]Bi_4$ (**C**)[21], was synthesized by combining K, Ga and Bi in stoichiometric amounts in a niobium ampoule. The ampoule was sealed by arc-welding, placed in an oven and kept at 900 °C for 48 h. The same steps were applied to synthesize a phase with the nominal composition '$K_2Tl_1Bi_3$'. Upon extraction of '$K_2Tl_1Bi_3$' with en/crypt-222, filtration and subsequent removal of the solvent, $[K(crypt\text{-}222)]_2(TlBi_3)\cdot 0.5en$ (**D**) was obtained in crystalline form[65]. A similar procedure employing a solid mixture of the nominal composition '$K_1Pb_1Bi_1$' yielded crystalline $[K(crypt\text{-}222)]_2(Pb_2Bi_2)\cdot en$ (**E**)[66]. $ThCl_4$ was synthesized according to the literature procedure[67]. Samples were shielded from ambient light throughout cluster syntheses. Note that all compounds comprising cluster anions **1**–**4** are air-sensitive.

Synthesis of $[ThCp^{\neq}{}_3Cl]$ (1). Compound **1** was prepared by metathesis reaction of $ThCl_4$ with $KCp^{\neq}$ ($Cp^{\neq}$ = 2,3,4,5-tetramethyl cyclopentadienyl, C_5Me_4H). $ThCl_4$ (3.065 g, 8.20 mmol) and $KCp^{\neq}$ (4.00 g, 25 mmol) were suspended in 300 ml of tetrahydrofuran at −78 °C. The mixture was allowed to reflux for a few hours. Soxhlet extraction of the crude, slightly yellow solid led to the extraction of 1.421 g (27.5%) of single-crystalline compound **1**.

Synthetic protocol of $[K(crypt\text{-}222)]_4[Th@Bi_{12}]\cdot 2en$ (2). The reactants for **2** were $K_5Ga_2Bi_4$ (**A**, 70 mg, 60 µmol), crypt-222 (113 mg, 300 µmol) and $[ThCp^{\neq}{}_3Cl]$ (19 mg, 30 µmol). The components were combined in a Schlenk tube and dissolved in 4 ml of en. An intense green solution formed initially, indicating the formation of bluish-green Bi_4^{2-} (ref. [21]). After stirring for 2 h, the solution was filtered through densely packed glass wool, carefully layered with toluene (5 ml) and stored for crystallization at 5 °C. After 10 days, crystals of **2** suitable for single-crystal X-ray diffraction formed at the wall of the Schlenk tube in ~20% yield. Identified by-products are $[K(crypt\text{-}222)]_2(GaBi_3)$ (**B**) and $[K(crypt\text{-}222)]Bi_4$ (**C**) in some cases, in varying yields.

Synthetic protocol of further Th-centred clusters. To demonstrate the particular role of the Ga/Bi elemental combination in this synthetic route, we performed analogous reactions of $[K(crypt\text{-}222)]_2(TlBi_3)\cdot en$ (**D**, 200 mg 118 µmol) and $[K(crypt\text{-}222)]_2(Pb_2Bi_2)\cdot en$ (**E**, 224 mg, 130 µmol) with $[ThCp^{\neq}{}_3Cl]$ (37 mg, 59 µmol or 20 mg, 30 µmol) under otherwise identical reaction conditions. This resulted in the formation of the actinide-centred clusters $[Th@Tl_2Bi_{11}]^{3-}$ (**3A**) and $[Th@Pb_2Bi_9]^{3-}$ (**4A**), in their corresponding $[K(crypt\text{-}222)]^+$ salts $[K(crypt\text{-}222)]_3[Th@Tl_2Bi_{11}]\cdot tol$ (**3**) and $[K(crypt\text{-}222)]_3[Th@Pb_4Bi_9]$ (**4**), both of which are known spherical cluster topologies. Compound **3** formed in 80% yield, and compound **4** formed as a minor product alongside re-crystallized precursor $[K(crypt\text{-}222)]_2(Pb_2Bi_2)\cdot en$ and crystals of $[K(crypt\text{-}222)]_2(Pb_7Bi_2)\cdot en$[66].

Single-crystal X-ray diffraction data. The data for the X-ray structural analyses were collected at 100(2) K with Cu-Kα radiation (λ = 1.54186 Å) on an area detector system (STOE StadiVari; compounds **1**, **2** and **3**) or with Mo-Kα radiation (λ = 0.7107 Å) on an imaging plate detector system (STOE IPDS II; compound **4**). The structures were solved by dual space methods (SHELXT)[68]. The refinement was done by full-matrix least-squares methods against F^2 with the program SHELXL[69]. The crystal data and experimental parameters of the structure determination are collected in Supplementary Table 1. Unit cell plots of the crystal structures are provided in Supplementary Fig. 1 (compound **1**), Supplementary Fig. 2 (compound **2**), Supplementary Fig. 3 (compound **3**) and Supplementary Fig. 4 (compound **4**).

Powder X-ray diffraction. The powder X-ray diffraction pattern of the crystalline material obtained at the synthesis of **2** was measured on a STOE StadiMP diffractometer system equipped with a Mythen 1K silicon strip detector and a Cu-Kα radiation source (λ = 1.54056 Å). An as-prepared sample of **1** was filled into a glass capillary (0.5-mm diameter), which was then sealed air-tight with soft wax. The tube was then mounted onto the goniometer head using wax (horizontal set-up) and rotated throughout the measurements. The diffraction diagram is shown in Supplementary Fig. 5. It exhibits compound **2** together with a related crystalline phase, most probably upon loss of crystal solvent in situ.

µ-XFS. All µ-XFS measurements were performed with a Bruker M4 Tornado, equipped with a Rh-target X-ray tube and a silicon drift detector. The emitted fluorescence photons were detected with an acquisition time of 100 s. Quantification of the elements was achieved through deconvolution of the spectra. The results are shown in Supplementary Figs. 6–8 and summarized in Supplementary Table 2.

ESI-MS. ESI mass spectra (Supplementary Figs. 9–11) were recorded with a Thermo Fisher Scientific Finnigan LTQ-FT spectrometer in negative ion mode. Single crystals of compounds **2**–**4** were dissolved in freshly distilled DMF inside a glovebox. The solutions were injected into the spectrometer with gas-tight 250-µl Hamilton syringes by syringe pump infusion. All capillaries within the system were washed with dry DMF for 2 h before and at least 10 min in between measurements to inhibit decomposition reactions and consequent clogging. The spectra are shown in Supplementary Figs. 9–11.

Magnetic measurements. The magnetic measurements on compound **2** were carried out with the use of a Quantum Design MPMS-XL SQUID magnetometer, which operates between 1.8 and 400 K with magnetic field up to 7 T. Measurements were performed on polycrystalline samples of **2** (29.1 and 11.9 mg) sealed in a polyethylene bag (29.7 and 31.4 mg) and prepared under a nitrogen atmosphere. Before the experiments, the field-dependent magnetization was measured at 100 K to confirm the absence of any bulk ferromagnetic impurities. The magnetic data were corrected for the sample holder. As shown in the χ versus T plot in Supplementary Fig. 12, compound **2** is reproducibly diamagnetic over the whole range of temperature between 1.85 and 300 K. The susceptibility at room temperature, $-0.0019\,cm^3\,mol^{-1}$, is close to the expected diamagnetic value of $-0.5\times MW\times 10^{-6} = -0.0023\,cm^3\,mol^{-1}$ intrinsic to the constituting atoms (MW, molecular weight). The small increase of the susceptibility below 10 K is compatible with a Curie law for 0.5% of an $S = 1/2$ spin (considering the MW of **2**). This type of Curie law, usually above 1%, is quasi-systematically observed in diamagnetic compounds and is the signature of defects or impurities that are easy to observe at low temperatures.

Quantum chemical calculations. Calculations were done with TURBOMOLE[48,49], both employing ECPs and scalar-relativistic all-electron approaches within the one-component local variant of the X2C Hamiltonian[60–63]. For details, see Supplementary Information. Magnetically induced current densities were obtained with the GIMIC) code[59] using the perturbed density[70] from TURBOMOLE.

The TURBOMOLE quantum program suite is available from https://www.turbomole.org (retrieved 29 August 2020), and the GIMIC code can be obtained from the GitHub repository at https://github.com/qmcurrents/gimic (retrieved 29 August 2020; open-source; see also ref. [69]). The GitHub repository also includes a sample input for GIMIC.

Further details are provided in the Supplementary Information, as well as a short note on the use of GIMIC with Python version 2.

References

65. Lichtenberger, N., Spang, N., Eichhöfer, A. & Dehnen, S. Between localization and delocalization: $Ru(cod)^{2+}$ units in the Zintl clusters $[Bi_9\{Ru(cod)\}_2]^{3-}$ and $[Tl_2Bi_6\{Ru(cod)\}]^{2-}$. *Angew. Chem. Int. Ed.* **56**, 13253–13258 (2017).
66. Ababei, R. et al. Making practical use of the pseudo-element concept: an efficient way to ternary intermetalloid clusters by an isoelectronic Pb^-–Bi combination. *Chem. Commun.* **48**, 11295–11297 (2012).
67. Deubner, H. L., Rudel, S. S. & Kraus, F. A simple access to pure thorium(IV) halides ($ThCl_4$, $ThBr_4$ & ThI_4). *Z. Anorg. Allg. Chem.* **643**, 2005–2010 (2017).
68. Sheldrick, G. M. SHELXT—integrated space-group and crystal-structure determination. *Acta Crystallogr. A Found. Adv.* **71**, 3–8 (2015).
69. Sheldrick, G. M. Crystal structure refinement with SHELXL. *Acta Crystallogr. C Struct. Chem.* **71**, 3–8 (2015).
70. Reiter, K., Mack, F. & Weigend, F. Calculation of magnetic shielding constants with meta-GGA functionals employing the multipole-accelerated resolution of the identity: implementation and assessment of accuracy and efficiency. *J. Chem. Theory Comput.* **14**, 191–197 (2018).

Acknowledgements

We thank the German Research Foundation (Deutsche Forschungsgemeinschaft, DFG) for financial support within the framework of GRK 1782. We thank J.L. Vasco and M. Pyschik for help with the synthesis, S. Ivlev, B. Weinert, M. Marsch and R. Riedel for help with the diffraction experiments, and M. Hellwig for measuring the EDX spectra of **1**. We also thank K. Reiter and F. Dehnen for discussions. N.L. acknowledges a grant from Marburg University Research Academy (MARA). Y.J.F. is grateful to Fonds der Chemischen Industrie for general support of his PhD. studies (Kekulé fellowship), to the German Academic Exchange Service (Deutscher Akademischer Austauschdienst, DAAD) for a fellowship (grant no. 57438025) and to F. Furche for hosting. R.C. acknowledges support from the University of Bordeaux, the CNRS, the Region Nouvelle Aquitaine, the MOLSPIN COST action CA15128 and the GdR MCM-2.

Author contributions

A.R.E., N.L., R.J.W. and H.L.D. conceived and performed the synthetic experiments, collected single-crystal X-ray crystallographic data, solved and refined the structures, performed ESI-MS and prepared samples for further analyses. R.C. performed and analysed the magnetic measurements. F.W. performed the computational structure optimization and orbital analysis, and Y.J.F. studied the aromaticity and performed the TD-DFT calculations as well as the structure optimizations for Fig. 1. S.D., F.K. and F.W. supervised the work. All authors co-wrote the paper.

Supplementary Information

Substantial π-aromaticity of the anionic heavy-metal cluster $[Th@Bi_{12}]^{4-}$

Armin R. Eulenstein,[1,2] Yannick J. Franzke,[3,†] Niels Lichtenberger,[1,2] Robert J. Wilson,[1,2] H. Lars Deubner,[1] Florian Kraus,[1] Rodolphe Clérac,[4] Florian Weigend,[1]* and Stefanie Dehnen[1,2]*

[1] Fachbereich Chemie, Philipps-Universität Marburg, Hans-Meerwein-Str. 4, 35032 Marburg, Germany. E-Mail: dehnen@chemie.uni-marburg.de; florian.weigend@chemie.uni-marburg.de

[2] Wissenschaftliches Zentrum für Materialwissenschaften (WZMW), Philipps-Universität Marburg, Hans-Meerwein-Str. 6, 35032 Marburg, Germany.

[3] Institute of Physical Chemistry, Karlsruhe Institute of Technology (KIT), Kaiserstr. 12, 76131 Karlsruhe, Germany.

[4] Univ. Bordeaux, CNRS, Centre de Recherche Paul Pascal, UMR 5031, 33600 Pessac, France.

[†] Present address: Fachbereich Chemie, Philipps-Universität Marburg, Hans-Meerwein-Str. 4, 35032 Marburg, Germany.

These authors contributed equally: Armin R. Eulenstein, Yannick J. Franzke.

Contents

1. Supplementary Discussion on the Formation of Compound 2

We suggest that the reaction that led to the formation of compound **2** took place according to the following reaction schemes starting out from compound $K_5Ga_2Bi_4$ (**A**).[1] The latter has been known as a precursor for the formation and isolation of the Zintl salt $[K(crypt\text{-}222)]_2(GaBi_3)\cdot en$ (**B**), but notably, the use of isolated **B** alone does not lead to the formation of any isolable cluster compounds. When **A** is employed instead, we observe not only the formation of compound **2**, but also the intermediate formation of bluish-green Bi_4^{2-}.[2] Therefore, we assume that **A** served as a source of both Bi_4^{2-} and $(GaBi_3)^{2-}$ anions to form *in situ* upon extraction with en [equations (1) and (2)], hence allowing for compound **2** to form under the given reaction conditions from these two reactants and compound $[ThCp^{\#}{}_3Cl]$ (**1**) [equation (3)] (note that all compounds are given without crypt-222 or crystal solvent en for simplification):

$$K_5Ga_2Bi_4 + 3\ H_2N(CH_2)_2NH_2 \rightarrow K_2Bi_4 + 2\ Ga^0\downarrow + 3\ KHN(CH_2)_2NH_2 + {}^3/_2\ H_2\uparrow \quad (1)$$

$$K_5Ga_2Bi_4 + 3\ H_2N(CH_2)_2NH_2 \rightarrow K_2(GaBi_3) + Ga^0\downarrow + Bi^0\downarrow + 3\ KHN(CH_2)_2NH_2 + {}^3/_2\ H_2\uparrow \quad (2)$$

$$3\ K_2Bi_4 + K_2(GaBi_3) + [ThCp^{\#}{}_3Cl]\ (\mathbf{1}) \rightarrow K_4[Th@Bi_{12}]\ (\mathbf{2}) + 3\ KCp^{\#} + KCl + Ga^0\downarrow + 3\ Bi^0\downarrow \quad (3)$$

Compound **1** was previously prepared from $ThCl_4$[3] and $KCp^{\#}$ ($Cp^{\#}$ = 2,3,4,5-tetramethyl cyclopentadienyl, C_5Me_4H) as described in the main document. To demonstrate the particular role of the Ga/Bi elemental combination in this synthetic route, we performed analogous reactions of $[ThCp^{\#}{}_3Cl]$ (**1**) with $[K(crypt\text{-}222)]_2(TlBi_3)\cdot en$ (**C**)[4] and $[K(crypt\text{-}222)]_2(Pb_2Bi_2)\cdot en$ (**D**)[5] under otherwise identical reaction conditions. This resulted in the formation of the actinide-centred clusters $[Th@Tl_2Bi_{11}]^{3-}$ (**3A**) and $[Th@Pb_4Bi_9]^{3-}$ (**4A**), in their corresponding $[K(crypt\text{-}222)]^+$ salts **3** and **4**. Both compounds are isostructural with previously reported uranium analogues, with no significant differences in bond lengths or cluster geometries due to similar ionic radii of the central uranium and thorium atoms in a formal +IV oxidation state. We note that in the reaction of **1** with **D**, we did not observe the formation of a 14-vertex cluster, such as "$[Th@Pb_7Bi_7]^{3-}$" or "$[Th@Pb_8Bi_6]^{4-}$"; this stands in contrast to the corresponding reaction with the $[UCp^{\#}{}_3Cl]$, where 13-vertex and 14-vertext clusters co-crystallized. We attribute this to the smaller ionic radius of Th^{4+} relative to U^{3+}, which leads to a distinct preference for the smaller 13-atom cluster shell.[6-8]

2. Supplementary Information on X-Ray Diffraction

2.1. Supplementary Information on the Single-Crystal X-Ray Diffraction Studies

All hydrogen atoms were kept riding on calculated positions with isotropic displacement parameters $U = 1.2\ U_{eq}$ (or $1.5\ U_{eq}$ for methyl groups) of the bonding partners. Crystallographic data for the three structures reported in this paper have been deposited with the Cambridge Crystallographic Data Centre as supplementary publications nos. CCDC-1983070 (**1**), CCDC-1983072 (**2**), CCDC-1983073 (**3**), CCDC-1983071 (**4**). The crystal data and experimental parameters of the structure determinations are collected in **Supplementary Table 1**.

Supplementary Table 1 | Crystal data and details of the structure determinations of 1-4.

Compound	**1**	**2**	**3**	**4**
empirical formula	$C_{27}H_{39}ClTh$	$C_{76}H_{156}Bi_{12}K_4N_{12}O_{24}Th$	$C_{42}N_4O_{12}K_3Tl_2Bi_{11}Th$	$C_{43}N_4O_{12}K_3Pb_4Bi_9Th$
nominal formula	$C_{27}H_{39}ClTh$	$C_{76}H_{156}Bi_{12}K_4N_{12}O_{24}Th$	$C_{61}H_{116}N_6O_{18}K_3Tl_2Bi_{11}Th$	$C_{61}H_{116}N_6O_{18}K_3Pb_4Bi_9Th$
formula weight [g mol^{-1}]	631.07	4257.50	3809.32	4188.38
crystal colour, shape	colourless, plate	black, prism	black, block	black, block
crystal size [mm^3]	0.03×0.03×0.06	0.17×0.09×0.015	0.15×0.16×0.010	0.12×0.10×0.08
crystal system	cubic	triclinic	monoclinic	monoclinic
space group	*I*-43*d*	$P\bar{1}$	$P2_1/m$	$P2_1/m$
a [Å]	21.3159(3)	14.5025(2)	14.6434(1)	14.6520(3)
b [Å]		16.4157(2)	21.801(2)	21.970(4)
c [Å]		27.2255(4)	16.3934(2)	16.468(3)
α [°]		81.1720(10)		
β [°]		86.0500(10)	107.135(1)	107.80(3)
γ [°]		67.1600(10)		
V [Å^3]	9685.3(4)	5902.27(15)	5001.15(9)	5047.4(19)
Z / ρ_{calc} [g cm^{-3}]	16 / 1.731	2 / 2.540	2 / 2.530	2 / 2.511
μ [mm^{-1}]	($Cu_{K\alpha}$) 20.93	($Cu_{K\alpha}$) 40.064	($Cu_{K\alpha}$) 49.285	($Mo_{K\alpha}$) 23.908
absorption correction	numerical	numerical	numerical	numerical
θ range [°]	5.1 – 69.9	2.9 - 68.0	2.8 - 67.5	1.3 - 25.4
total reflns	20014	170346	150785	45407
unique reflns / [R_{int}]	1529 / 0.047	21314/ 0.109	9272/ 0.095	9511/ 0.179
obs. Reflns [$I > 2\sigma(I)$]	1389	14722	8068	6108
Parameters	92	1171	213	213
wR_2 (all data) / R_1 [$I > 2\sigma(I)$]	0.0247 / 0.0129	0.2324/ 0.0759	0.2312 / 0.0774	0.2395/ 0.0831
GooF (all data)	1.04	1.01	1.06	1.05
max peak/hole [e Å^{-3}]	0.23/ −0.31	4.80/ –3.64	7.56/ –3.54	3.81/ –4.20

2.2. Details of the Structure Determinations

2.2.1. Structure Determination of Compounds [ThCp$^{\#}_3$Cl] (1) and [K(crypt-222)]$_4$[Th@Bi$_{12}$]·2en (2)

Supplementary Fig. 1 provides the view of a section of the crystal structure of compound **1**, and **Supplementary Fig. 2** provides the view of a section of the crystal structure of compound **2**. The structure of **2** could be solved in the centrosymmetric triclinic space group $P\bar{1}$. It revealed one independent $[Th@Bi_{12}]^{4-}$ anion with pseudo-symmetry D_{3h} (see **Fig. 2** in the main document). Remaining electron density is mainly located in close proximity to the heavily absorbing Th and Bi atoms and is an effect of absorption that could not be resolved by different absorption correction techniques ($\mu = 40 mm^{-1}$), in addition to termination effects near the heavy atoms.

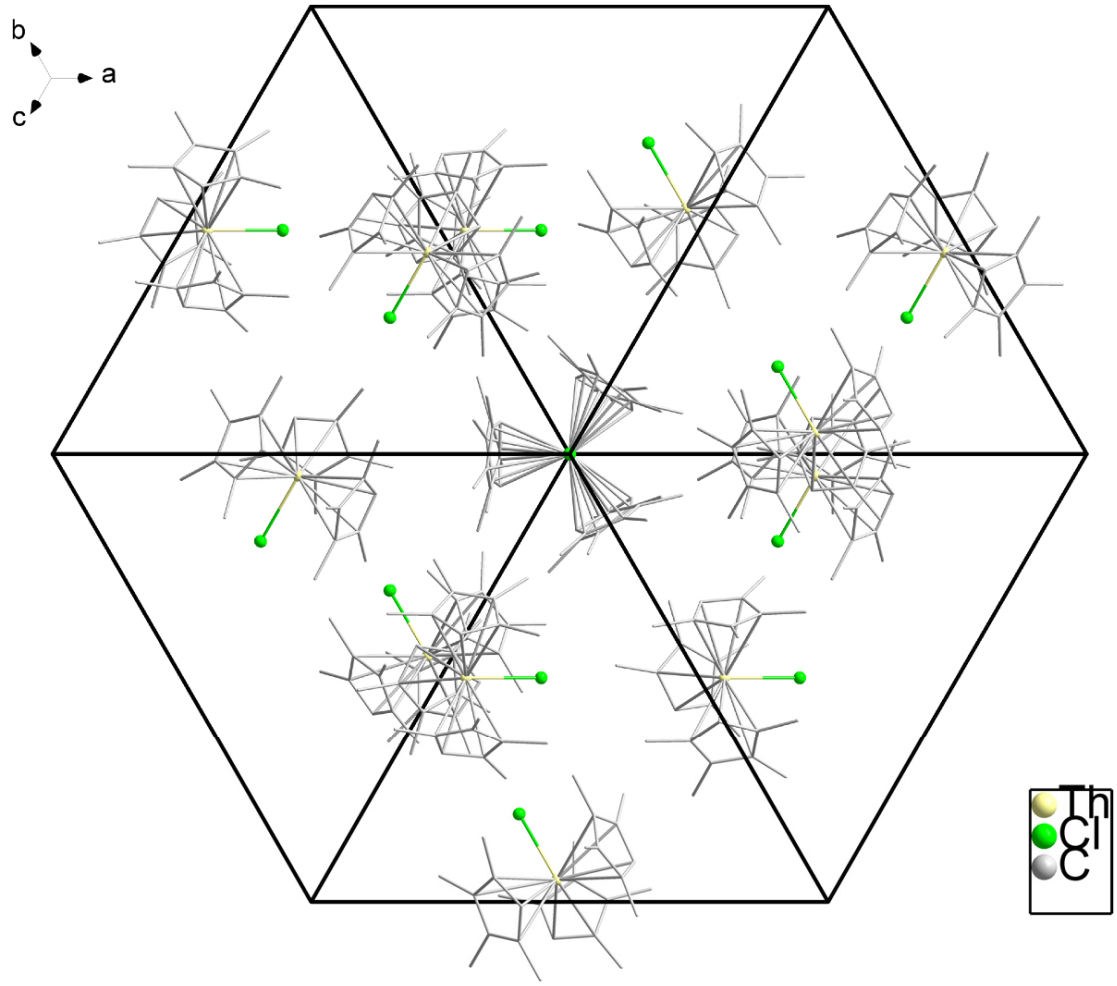

Supplementary Fig. 1 | Section of the crystal structure of compound 1. View along the crystallographic <111> direction. H atoms are omitted.

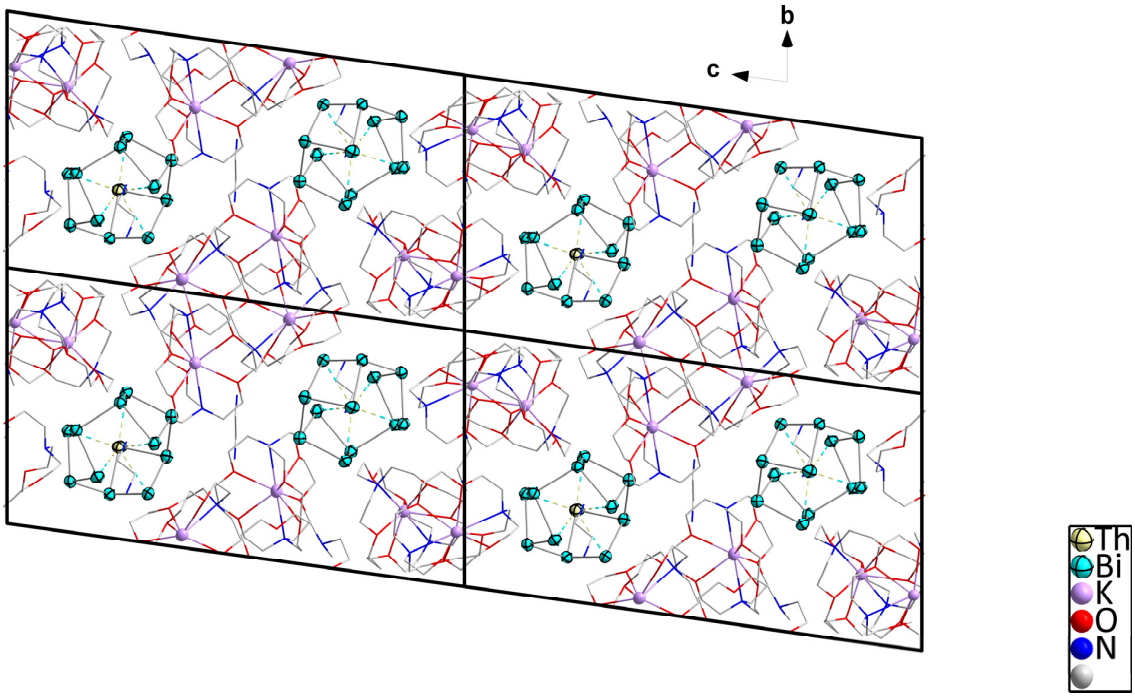

Supplementary Fig. 2 | Section of the crystal structure of compound 2. View along the crystallographic *a* direction. H atoms are omitted.

2.2.2. Structural Models of Compounds [K(crypt-222)]$_3$[Th@Tl$_2$Bi$_{11}$]·tol (3) and [K(crypt-222)]$_3$[Th@Pb$_4$Bi$_9$]·tol (4)

Supplementary Fig. 3 provides the view of a section of the crystal structure of compound 3, and **Supplementary Fig. 4** provides the view of a section of the crystal structure of compound 4.

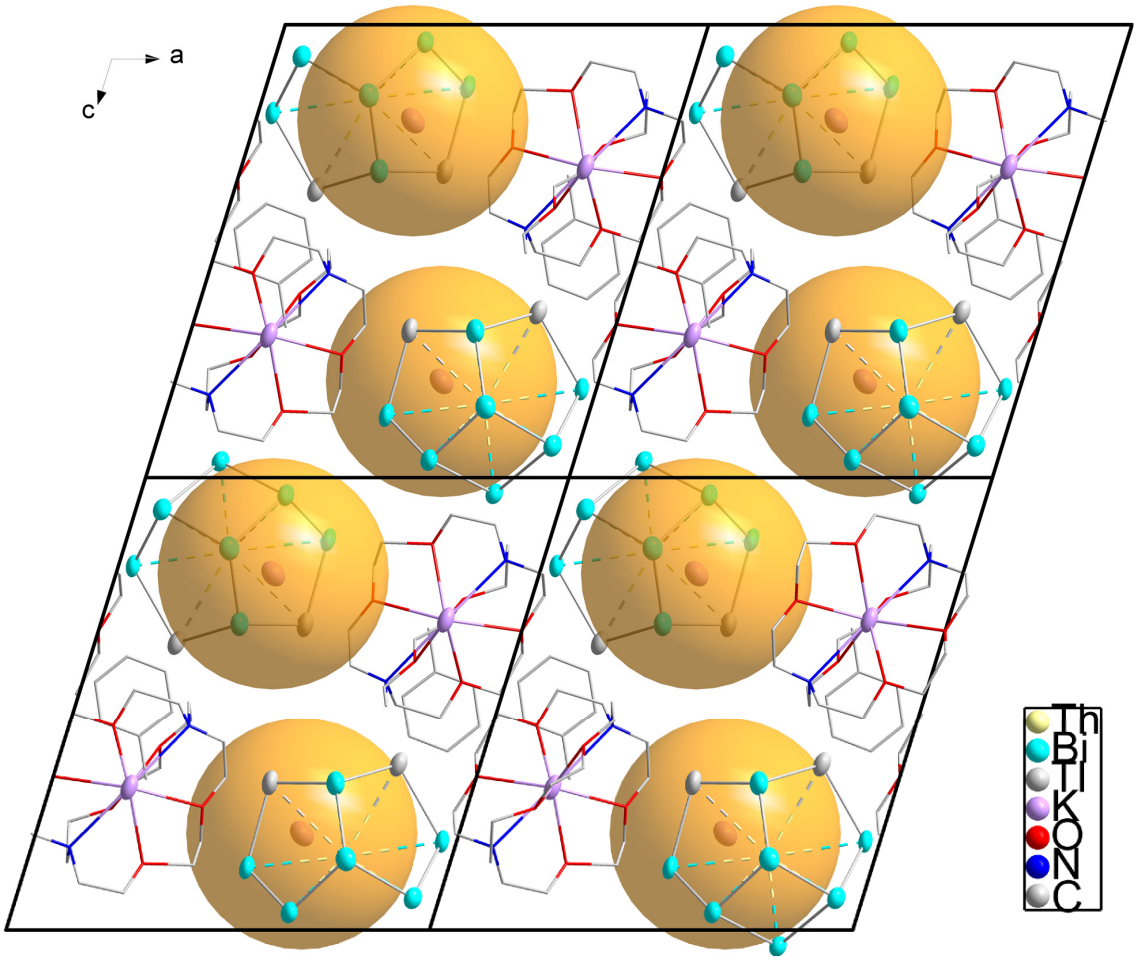

Supplementary Fig. 3 | Section of the crystal structure of compound 3. View along the crystallographic *b* direction. H atoms are omitted. Not modelled electron density of crypt-222 molecules are indicated by semi-transparent spheres.

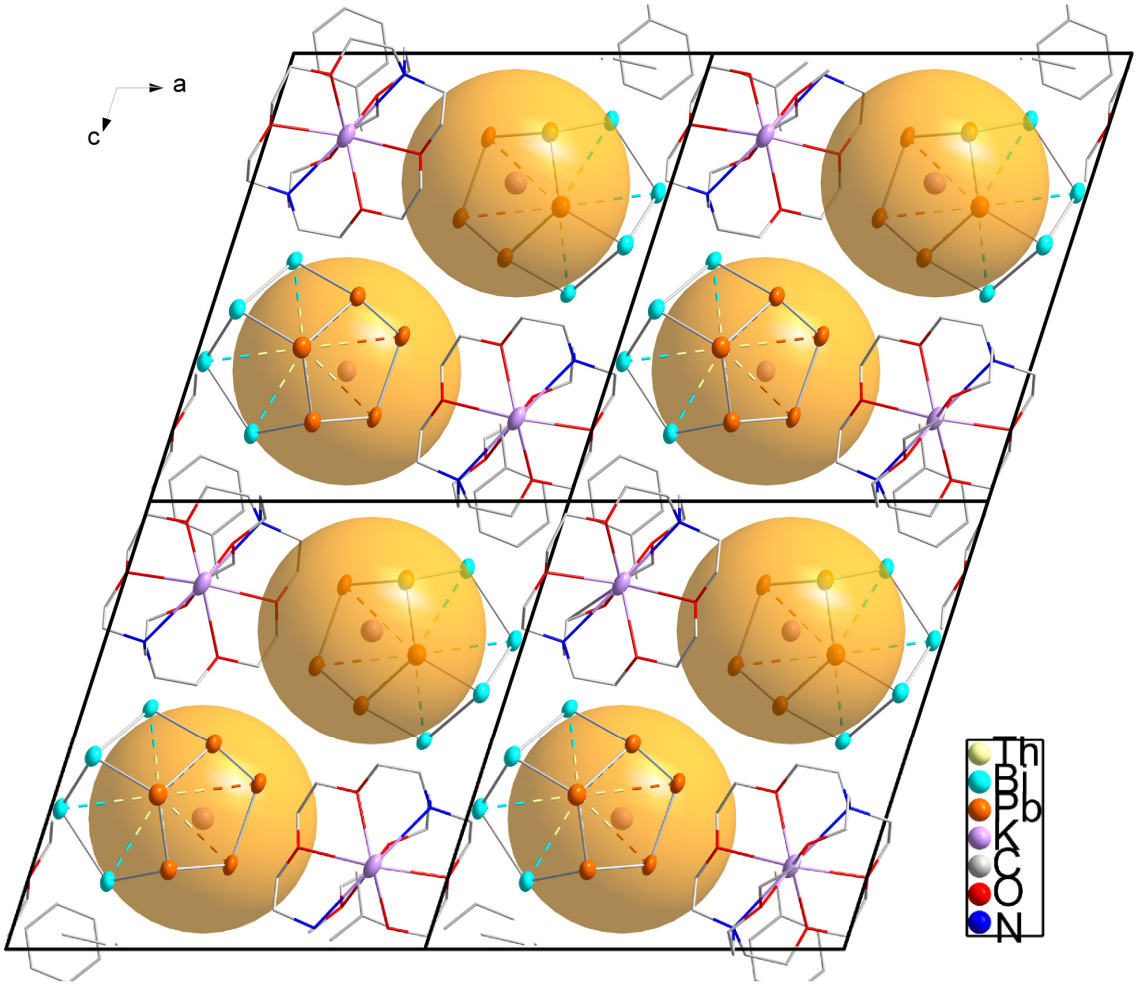

Supplementary Fig. 4 | Section of the crystal structure of compound 4. View along the crystallographic *b* direction. H atoms are omitted. Not modelled electron density of crypt-222 molecules are indicated by semi-transparent spheres.

For compounds **3** and **4**, the solvent mask as implemented in Olex 2-1.3 was applied for one not localizable crypt-222 molecule per compound.[9] For compound **3**, the total solvent accessible volume / cell amounts to 1673.3 Å^3 [33.5%], the total electron count / cell is 196.8. For compound **4**, the total solvent accessible volume / cell amounts to 1684.1 Å^3 [33.4%], the total electron count / cell is 97.7.

2.2.3. Responses to A-Level and B-Level Alerts in the CIFs of Compounds 2, 3, and 4

Responses to A-level and B-level alerts in the CIF of compound $[K(crypt\text{-}222)]_4[Th@Bi_{12}]\cdot 2en$ (2)

PROBLEM: Large Hirshfeld Difference C8DA--C7DA 0.32 Ang.
RESPONSE: This is due to heavy disorder of the organic molecules in the crystal structure, which was modelled by split positions that produce small distances between (non-bonded) atoms on these disorder positions.

PROBLEM: Isolated Metal Atom found in Structure (Unusual) Bi02 Check
RESPONSE: The distance between Bi atoms are not properly recognized by the program.

PROBLEM: Single Bonded Metal Atom in Structure (Unusual) Bi05 Check
RESPONSE: The distance between Bi atoms are not properly recognized by the program.

PROBLEM: Low Bond Precision on C-C Bonds ..... 0.03974 Ang.
RESPONSE: This is due to high mobility of the cryptand molecules in the crystal and corresponding disorder problems.

PROBLEM: Check Calcd Resid. Dens. 1.01A From Th01 4.76 eA-3
RESPONSE: Residual electron density close to heavily absorbing Bi and Th atoms is no sign of disorder but a mere artefact of the high absorption of the sample and Fourier ripples.

PROBLEM: Check Calcd Resid. Dens. 0.68A From Bi0B -3.67 eA-3
RESPONSE: Residual electron density close to heavily absorbing Bi and Th atoms is no sign of disorder but a mere artefact of the high absorption of the sample and Fourier ripples.

Responses to A-level and B-level alerts in the CIF of compound $[K(crypt\text{-}222)]_3[Th@Tl_2Bi_{11}]\cdot tol$ (3)

PROBLEM: Low Bond Precision on C-C Bonds ..... 0.05182 Ang.
RESPONSE: This is due to high mobility of the cryptand molecules in the crystal and corresponding disorder problems.

Responses to A-level and B-level alerts in the CIF of compound $[K(crypt\text{-}222)]_3[Th@Pb_4Bi_9]\cdot tol$ (4)

PROBLEM: Isotropic non-H Atoms in Main Residue(s) ..... 26 Report
RESPONSE: These atoms belong to disordered cryptand molecules, for which anisotropic refinement led to worse result.

PROBLEM: Low Bond Precision on C-C Bonds ..... 0.04063 Ang.
RESPONSE: This is due to high mobility of the cryptand molecules in the crystal and corresponding disorder problems.

2.3 Powder X-Ray Diffraction of Compound 2

Deviations between the measured diffraction pattern and the pattern simulated based on the single-crystal data can be attributed to two major reasons. First, grinding of the crystals leads to a smeary solid, indicating that the crystals readily release solvent molecules (an observation that is often made for Zintl salts comprising crystal solvent), which commonly leads to the formation of related compounds with fewer crystal solvent, even *in situ* (a famous example for the co-existence of such compounds with different solvent content is the double salt $[K(crypt\text{-}222)]_6[In_4Bi_5][In_4Bi_5]\cdot 1.5en\cdot 0.5tol$).[1] Second, this procedure at the same time enhances the background, and it changes the relative intensities in addition to inherent texture effects. Co-crystallization of the interim precursors $[K(crypt\text{-}222)]_2(GaBi_3)$[1] and $[K(crypt)]_2Bi_4$[5] is sometimes observed under the given reaction conditions (see Methods section in the main document), yet in this sample, the reflections were not detected.

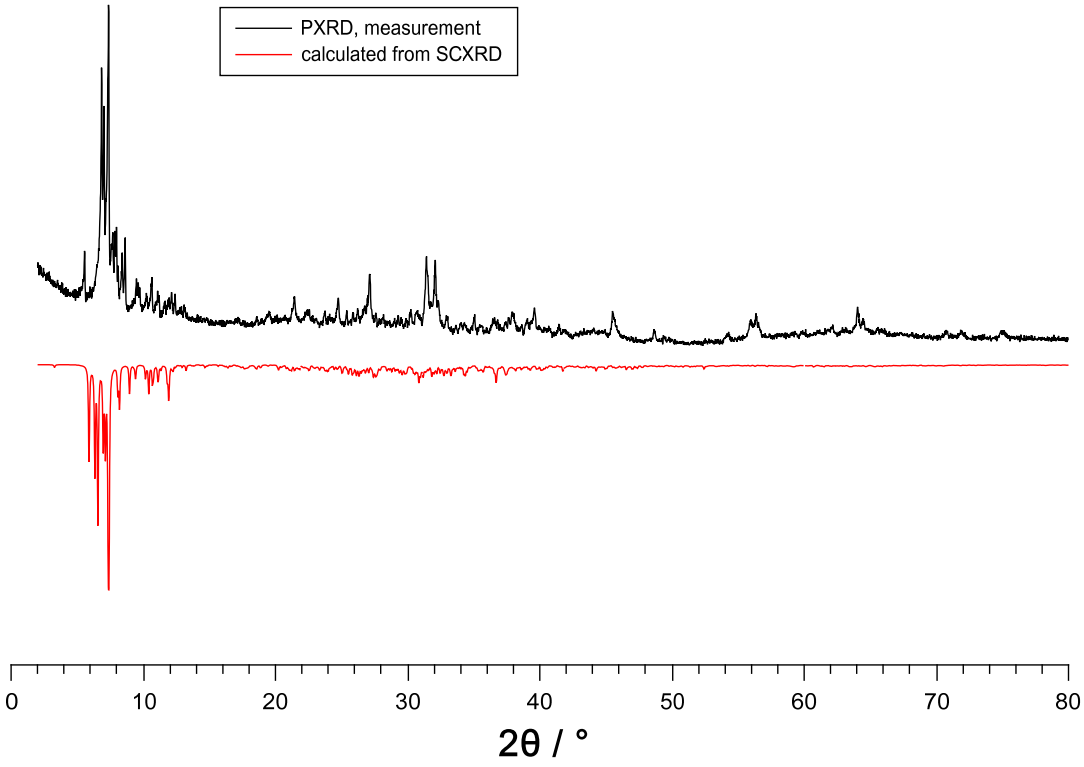

Supplementary Fig. 5 | Powder X-ray diffraction diagram of compound 2. The black line shows the measured diffraction pattern, the red line represents the diffraction pattern simulated from the single-crystals X-ray diffraction data.

3. Supplementary Information on Micro-X-Ray Fluorescence Spectroscopy (μ-XFS)

Results of the μ-XFS measurements are summarized in **Supplementary Table 2**, corresponding spectra are shown in **Supplementary Figs. 6**, **7**, and **8**. The data of compound **2** was collected on the same crystal from which single crystal X-ray diffraction data was collected. Several measurements produced unreasonable deviation of the K versus Bi amounts. We assume that this is due to beginning corrosion on the crystal surface upon exposure during sample preparation. This is frequently observed for air-sensitive compounds, and also affects the data obtained for the other elements.

Supplementary Table 2 | μ-XFS analysis of 2 (K, Bi, Th), 3 (K, Tl, Bi, Th), and 4 (K, Pb, Bi, Th).

Element	Element wt %	Weight % err. (1 sigma)	Atom %	Atom % calc.	Absolute deviation.
			$[K(crypt\text{-}222)]_4[Th@Bi_{12}]\cdot 2en$ (**2**)		
K-K	8.72	0.01	37.85	23.53	+14.32%
Bi-L	88.58	0.01	58.91	70.59	-11.68%
Th-L	2.71	0.01	3.24	5.88	-2.64%
Total	100.01		100.00	100.00	
			$[K(crypt\text{-}222)]_3[Th@Tl_2Bi_{11}]\cdot tol$ (**3**)		
K-K	5.18	0.01	22.57	17.65	+4.92%
Tl-L	14.28	0.01	11.91	11.76	+0.15%
Bi-L	78.29	0.01	63.86	64.71	-0.85%
Th-L	2.26	0.01	1.66	5.88	-4.22%
Total	100.01		100.00	100.00	
			$[K(crypt\text{-}222)]_3[Th@Pb_4Bi_9]\cdot tol$ (**4**)		
K-K	4.17	0.00	18.92	17.65	+1.27%
Pb-L	27.39	0.00	23.44	23.53	-0.09%
Bi-L	63.48	0.00	53.86	52.94	+0.92%
Th-L	4.95	0.00	3.78	5.88	-2.1%
Total	99.99		100.00	100.00	

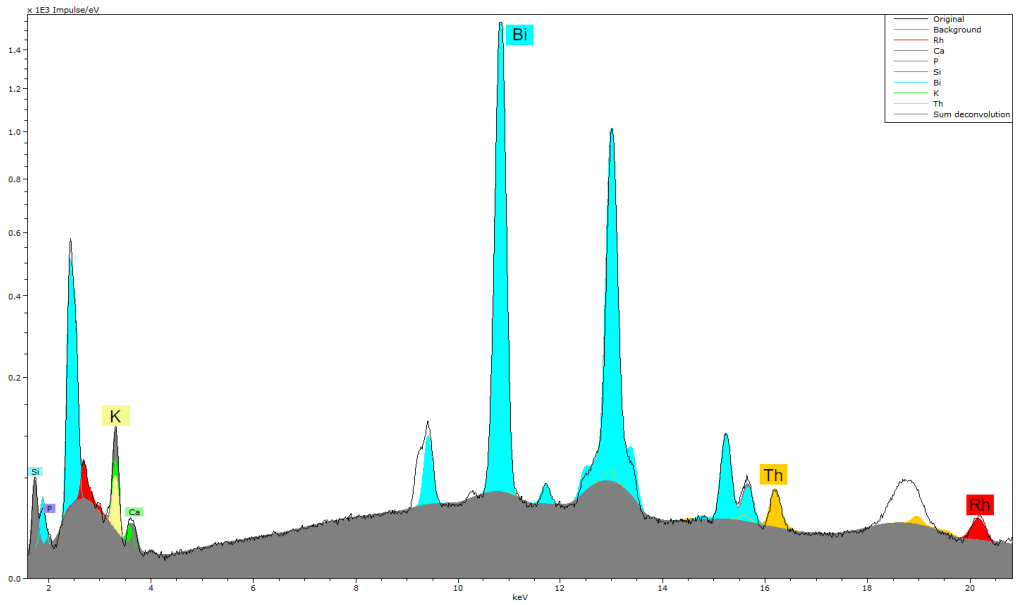

Supplementary Fig. 6 | *μ*-XFS spectrum of 2 (line) with the results of the deconvolution algorithm (solid, coloured). Colours are used as follows: K (yellow), Bi (turquoise), Th (orange). Note, that the intensity is displayed on a square root scale to allow for a better visibility of small features in the spectrum.

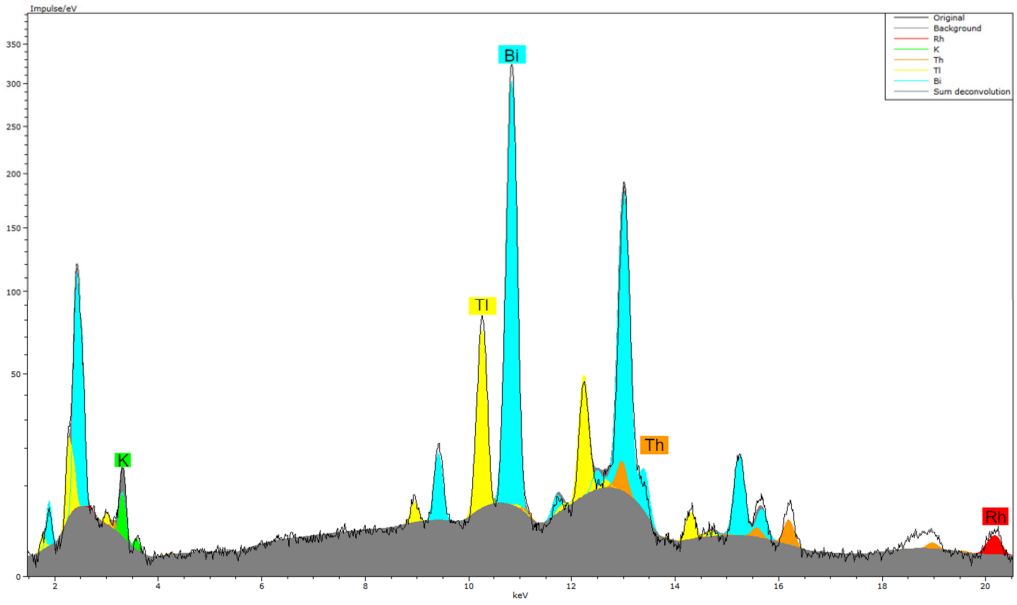

Supplementary Fig. 7 | *μ*-XFS spectrum of 3 (line) with the results of the deconvolution algorithm (solid, coloured). Colours are used as follows: K (green), Bi (turquoise), Th (orange), Tl (yellow). Note, that the intensity is displayed on a square root scale to allow for a better visibility of small features in the spectrum.

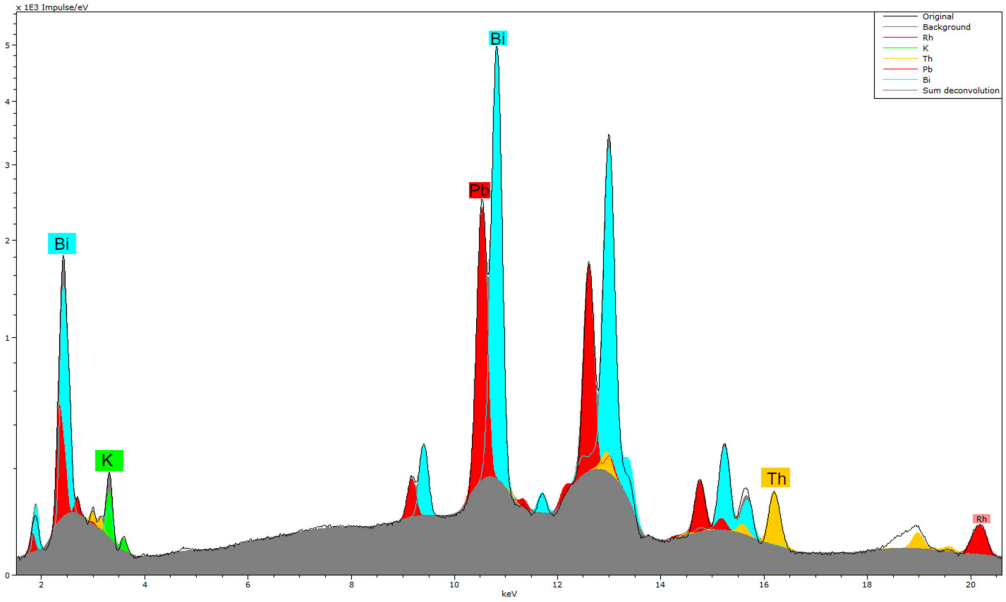

Supplementary Fig. 8 | *μ*-XFS spectrum of 4 (line) with the results of the deconvolution algorithm (solid, coloured). Colours are used as follows: K (green), Bi (turquoise), Th (orange), Pb (red). Note, that the intensity is displayed on a square root scale to allow for a better visibility of small features in the spectrum.

4. Supplementary Information on Electrospray Ionization (ESI) Mass Spectrometry

4.1. ESI Mass Spectrum of $[K(crypt\text{-}222)]_4[Th@Bi_{12}]\cdot 2en$ (2)

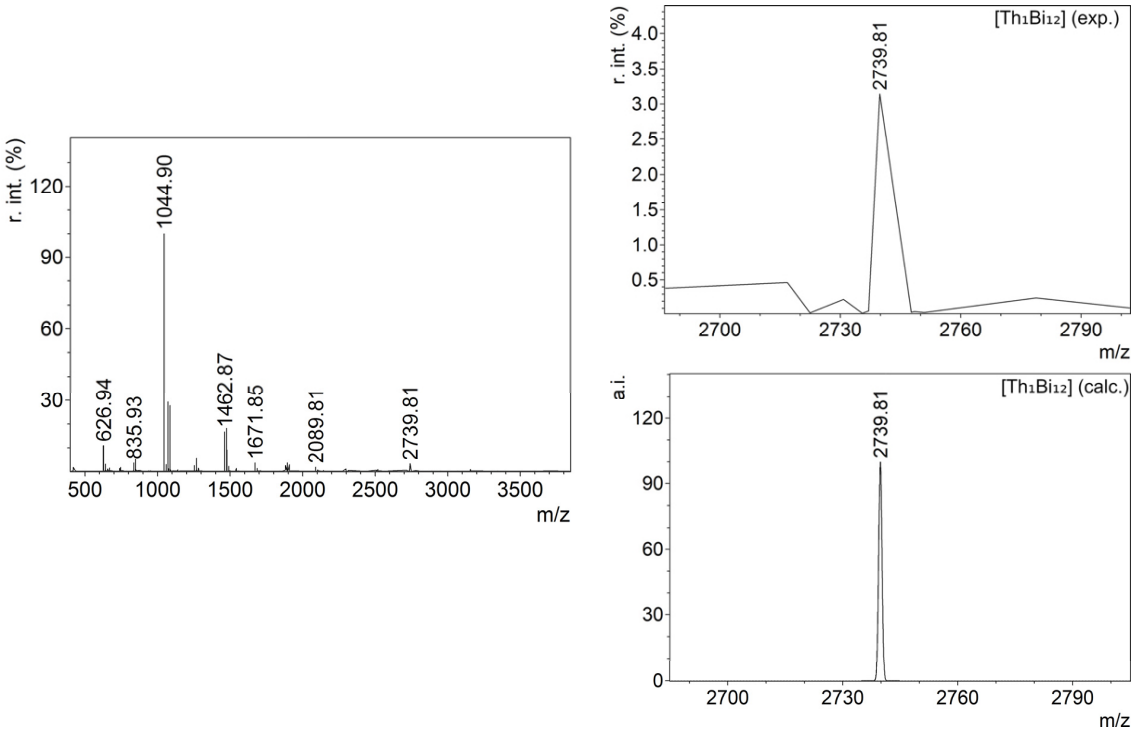

Supplementary Fig. 9 | High resolution ESI mass spectrum in negative ion mode of a solution of 2 in DMF. Left: overview spectrum between 400 and 4000 m/z with the labelled peaks being polybismuthide fragments Bi_3^-, Bi_5^-, Bi_6^-, Bi_7^-, Bi_8^-, Bi_{10}^-, and $[ThBi_{12}]^-$, in ascending order (from left). Right: Close-up of the peak of $[ThBi_{12}]^-$ (top: measured; bottom: calculated).

4.2. ESI Mass Spectrum of $[K(crypt\text{-}222)]_3[Th@Tl_2Bi_{11}]\cdot tol$ (3)

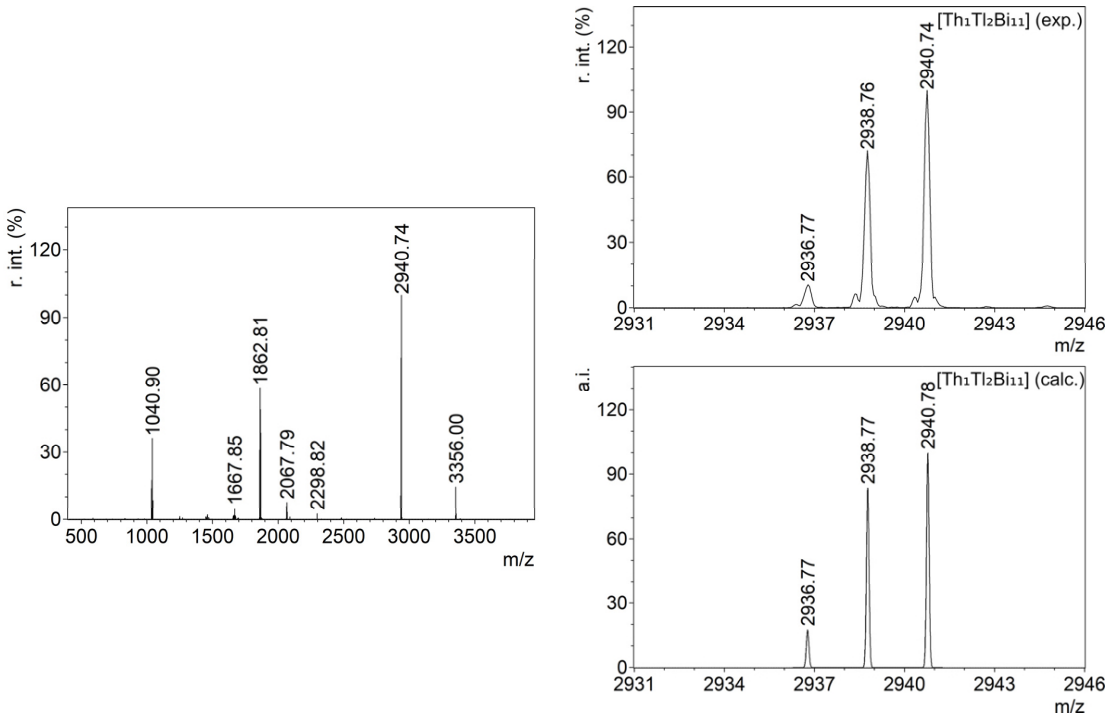

Supplementary Fig. 10 | High resolution ESI mass spectrum in negative ion mode of a solution of 3 in DMF. Left: overview spectrum between 400 and 4000 m/z. Right: Close-up of the peak of $[ThTl_2Bi_{11}]^-$ (top: measured m/z pattern; bottom: calculated m/z pattern).

4.3. ESI Mass Spectrum of $[K(crypt\text{-}222)]_3[Th@Pb_4Bi_9]\cdot tol$ (4)

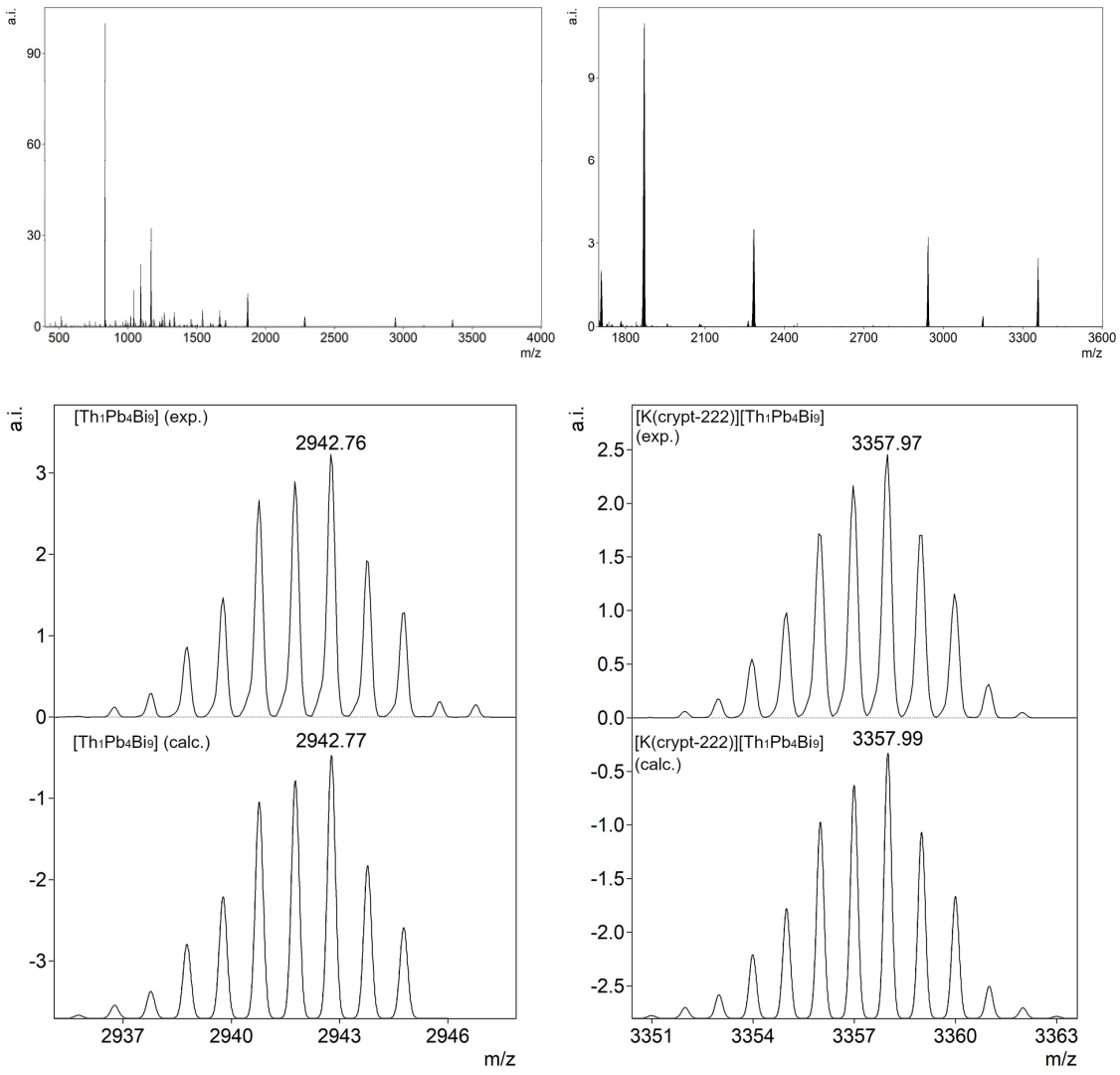

Supplementary Fig. 11 | High resolution ESI mass spectrum in negative ion mode of a solution of 4 in DMF. Top: overview spectra between 400 and 4000 m/z, and between 1700 and 3600 m/z, respectively. Bottom: Close-up of the peaks of $[ThPb_4Bi_9]^-$ (left) and $[K_1C_{18}N_2H_{36}O_6ThPb_4Bi_9]^-$ (right) with calculated m/z patterns shown below.

5. Supplementary Information on Magnetic Measurements of Compound 2

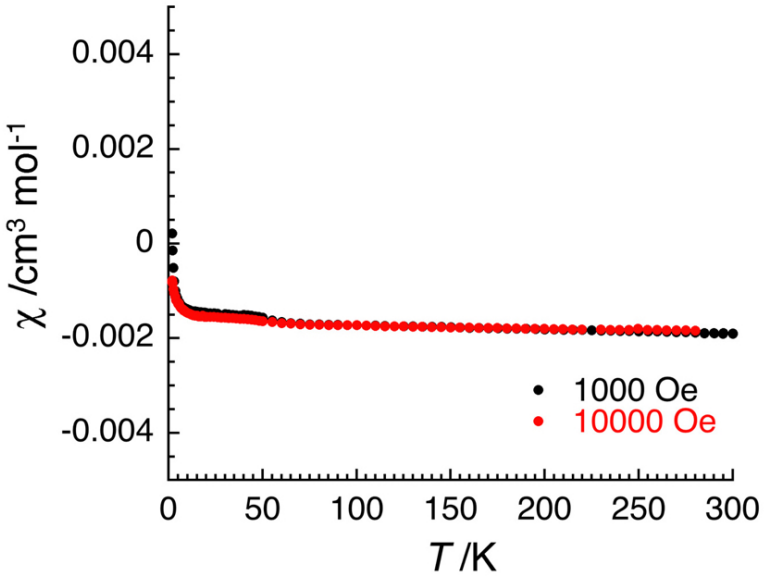

Supplementary Fig. 12 | Temperature dependence of the magnetic susceptibility, χ, at 0.1 and 1 T between 1.85 and 300 K. The susceptibility χ is defined as magnetic susceptibility equal to M/H per mole of the complex).

6. Supplementary Details on Quantum Chemical Investigations

6.1. Methods and Supplementary Results

Calculations were carried out with TURBOMOLE.[10-13] The structures of the molecules displayed in **Fig. 1** of the main text and related compounds were optimized with the PBE[14] functional. For molecules featuring light elements (up to Kr) only, the def2-TZVP basis[15] together the corresponding auxiliary basis sets[16] for the resolution of the identity approximation (RI-*J*). Medium sized grids[17] (gridsize 3) were used for the numerical integration of the exchange-correlation terms. The conductor-like screening model[18,19] (COSMO) was applied for charge compensation of the cations and anions with the default parameters. The dispersion corrections D3[20] and D4[21,22] were applied to the diborallyl cation due to the tert-butyl groups. Structures of molecules containing heavier elements were optimized with the scalar-relativistic exact two-component (X2C) Hamiltonian[23-25] in its local variant[26] (DLU-X2C) within the finite nucleus model (parameters taken from Ref. 27) using tailored grids[28] (gridsize 3a) and the x2c-TZVPall-s basis set[28] with the corresponding auxiliary basis.[29] Additionally, single point calculations of these compounds were carried out with the def2-TZVP (auxiliary) basis set and effective core potentials.[30,31] Tight self-consistent field (SCF) convergence thresholds of 10^{-8} E_h were used for all calculations and a threshold of 10^{-7} a.u. was used for the response of the orbitals (norm of the residuum) in the coupled-perturbed Kohn-Sham equations to calculate the perturbed density as part of a nuclear magnetic resonance (NMR) shielding calculation.[32] For Sb_4^{2-} and Bi_4^{2-}, calculations were further performed with the PBE0 hybrid functional[33] and also with the def2-TZVPPD basis set.[34] Ring currents and nucleus-independent chemical shifts[35] (NICS) were calculated analogously as outlined below for $[Th@Bi_{12}]^{4-}$. However, for S_2N_2, Se_4^{2+}, and Te_4^{2+} NICS(1) to NICS(5) were additionally calculated in line with Ref. 36. The results are listed in an additional supplementary file (Fig1-OptimizedStructures-GIMIC-NICS.txt).

The structure of $[Th@Bi_{12}]^{4-}$ was optimized with the following parameters. For Th, an effective core potential covering the 78 inner electrons (ECP-78)[37] was used together with a triple-zeta basis[37] (def-TZVP), for Bi an ECP-60[30] also with a triple-zeta basis[15] (def2-TZVP). COSMO[18,19] was applied for charge compensation with the default parameters. Structures were optimized using the PBE[14] functional and medium sized modified grids[17] (gridsize m3) together with a self-consistent field (SCF) convergence threshold of 10^{-7} E_h. The RI-*J* approximation was applied with the corresponding auxiliary basis sets.[16] The lowest triplet excitation energy based on time-dependent density functional theory[38-40] (TD-DFT) is 0.351 eV. A norm of the residuum of 10^{-6} a.u. ensures well-converged excitation vectors. Thus, no triplet instability is encountered.

Orbital localization was carried out with the Boys procedure[41] and the intrinsic bond orbital (IBO) method,[42] representative localized orbitals are shown in **Fig. 4b-4g** in the main document, and **Supplementary Fig. 13**. Atomic charge contributions to molecular orbitals were calculated with a Mulliken population analysis.[43] A comparison of the electron localization function[44] (ELF) of "$[Bi_{12}]^{6-}$" and "$[Bi_{12}]^{8-}$" is shown in **Supplementary Fig. 14**.

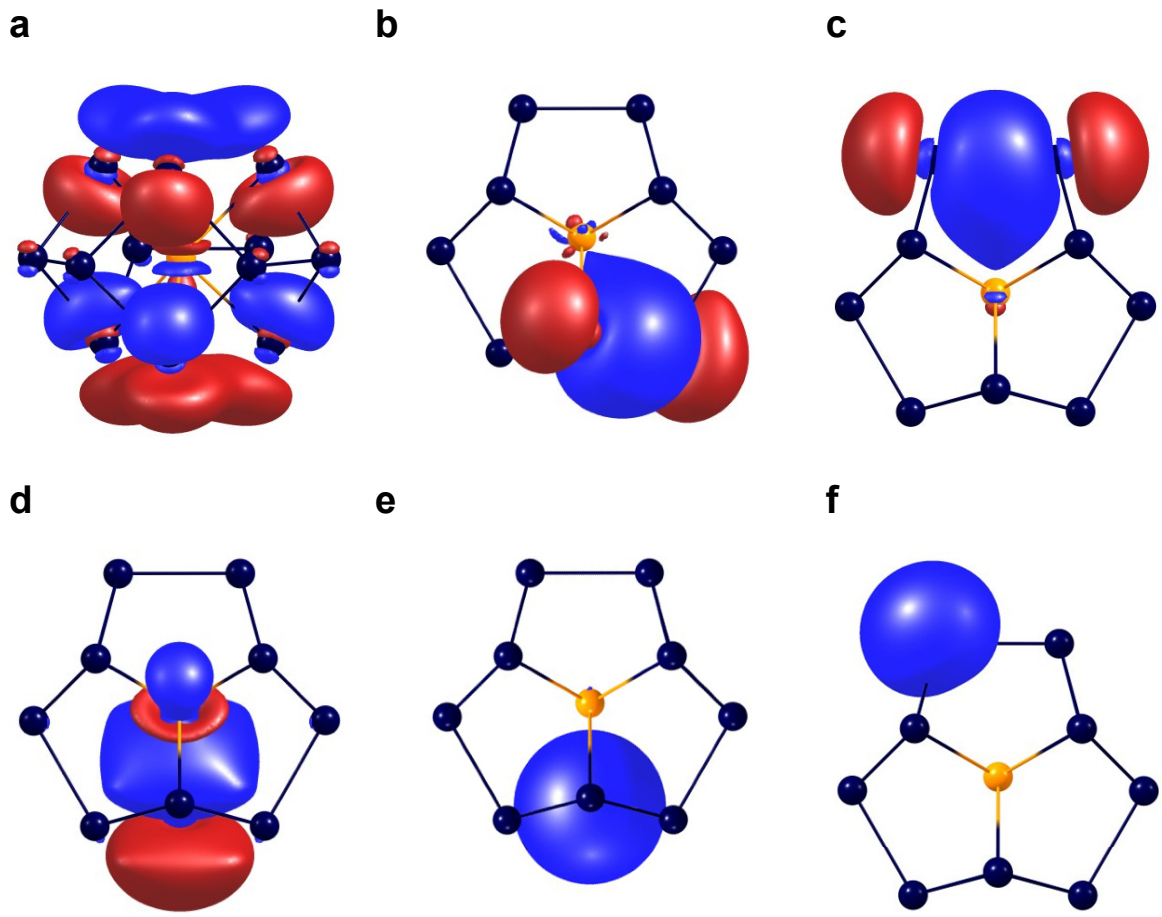

Supplementary Fig. 13 | Illustration of representative localized molecular orbitals of $[Th@Bi_{12}]^{4-}$ generated with the intrinsic bond orbital (IBO) method. a, IBO representing a non-localizable orbital of highest energy that is responsible for the π-aromaticity of compound **2** (side view). **b,** IBO representing a 2-center-2-electron (2c2e) Bi−Bi bond within a Bi_4 ring (top view). **c,** IBO representing a 2c2e Bi−Bi bond between two Bi_4 rings (top view). **d,** IBO representing a 2c2e Bi−Th bond (top view). **e,** IBO representing a lone pair at a Bi atom above/below the equatorial plane of the molecule (top view). **f,** IBO representing a lone pair found at a Bi atom within the equatorial plane of the molecule (top view). Contours are drawn at isovalues of ±0.021 a.u. in blue and red colour in each panel.

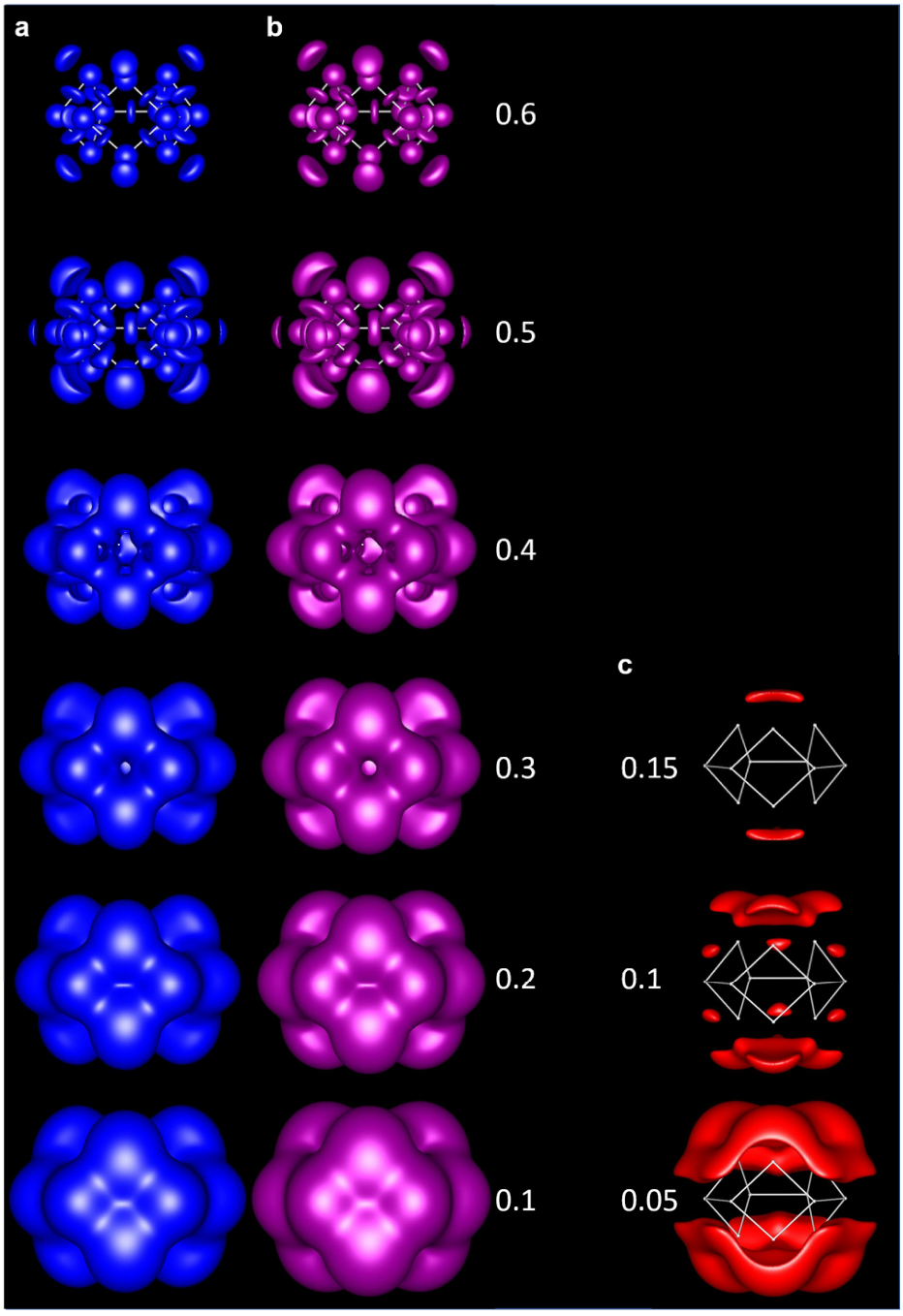

Supplementary Fig. 14 | Comparison of the electron localization function (ELF) of $\{Bi_{12}\}^{6-}$ and $\{Bi_{12}\}^{8-}$ at the def(2)-TZVP/PBE level. The molecule is placed in space corresponding to the orientation shown in **Fig. 2** (right hand side) in the main document. A value of 0.5 refers to the free electron gas. **a,** Illustration of ELF of $\{Bi_{12}\}^{6-}$, plotted at contour ELF values of 0.1 - 0.6 (in 0.1 steps). **b,** Illustration of ELF of $\{Bi_{12}\}^{8-}$, plotted at contour ELF values of 0.1 - 0.6 (in 0.1 steps). **c,** Plot of the difference of the ELF values in **a** and **b**, representing the delocalization of two of the total of 68 electrons in "Bi_{12}^{8-}", plotted at contour ELF values of 0.05, 0.1.

The magnetically induced current density was studied with the above ECPs, basis sets, and COSMO employing the BP86,[45,46] PBE,[14] TPSS,[47] and TPSSh[48] functional. Medium sized grids[17] (gridsize 3) were utilized for the numerical integration of the exchange correlation potential. Tight SCF convergence thresholds of 10^{-8} E_h were used and a threshold of 10^{-7} a.u. was used for the response of the orbitals in the coupled-perturbed Kohn-Sham equations to calculate the perturbed density as part of a NMR shielding calculation.[32] To study the effect of the relativistic Hamiltonian and the contribution of the core electrons to the ring current, the scalar-relativistic X2C Hamiltonian[23-25] was employed in its local variant[26] (DLU-X2C) within the finite nucleus model (parameters taken from Ref. 27) together with the segmented contracted Jorge-TZP-DKH,[49,50] taken from the basis set exchange library[51,52] and the decontracted Dyall-VTZ[53-56] basis set. Tailored grids[28] (gridsize 3a) were selected. Here, the RI-*J* approximation was not applied in the DLU-X2C calculations. The gauge-including magnetically induced current (GIMIC) code[57-59] was utilized to calculate the magnetically induced current density based on the derivative of the electron density with respect to the magnetic field and the Biot-Savart expressions of the NMR shielding constant. A diatropic current flow indicates an aromatic system whereas a paratropic current flow characterizes an antiaromatic compound according to the magnetic criterion of aromaticity.[59-61] The used version of GIMIC utilizes Python 3. For Python 2, the line 'from__future__import print_function' must be added to the header of the build version of turbo2gimic.py, which converts TURBOMOLE's (un)perturbed density matrices, structure, and basis set data to the GIMIC input. This allows Python 2.6 and 2.7 to interpret the Python 3 syntax of the print function.

The net current flow strength was obtained by numerical integration. Therefore, an integration plane was placed through the Bi_A–$Bi_{A'}$ bond parallel to the magnetic field, which is perpendicular to the molecular plane consisting of the Bi_A atoms and Th, as shown in **Supplementary Fig. 15**.

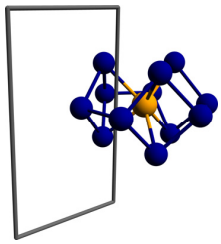

Supplementary Fig. 15 | Integration plane to calculate the current strength in order to quantify the degree of aromaticity. The integration plane was determined based on the magnetically induced current density profile for each level of theory.

The total net ring currents in **Supplementary Table 3** indicate aromaticity. A diatropic ring current of ca. 22 to 24 nA/T was found in the ECP calculations. This is roughly twice the ring current of benzene (11.4 nA/T at the PBE level) and close to the ring current of porphine and zinc porphyrin (25.3 and 25.0 nA/T at the PBE level). The application of the DLU-X2C Hamiltonian results in a slight increase of the net ring current by ca. 2-3 nA/T with the Jorge-TZP-DKH basis set. Therefore, $[Th@Bi_{12}]^{4-}$ is clearly aromatic based on the magnetic criterion. The Bi_{12}^{8-} ring sustains a net current flow of 23.4 nA/T at the ECP/BP86 level. Here, the integration plane starts at the centre of the ring. Similar to porphine,[62] all valence electrons of the Bi_{12}^{8-} framework are involved in the current flow. Thus, Th^{4+} is mainly required to stabilize the cluster, and of minor importance for the degree of aromaticity as it only changes the net ring current by ca. 3%. The ring current depends

on the number of electrons and the molecular structure. Hence, it is not a direct measure of aromaticity. But has proven to be a useful tool in numerous studies[60,62-65] and the ring current is a justification of aromaticity according to the International Union of Pure and Applied Chemistry[61] (IUPAC). Furthermore, we calculated the nucleus-independent chemical shifts[35] of the hypothetically "Bi_{12}^{8-}" at the centre of the cluster. The NICS and current strengths are reported in **Supplementary Table 4**. These results also indicate aromaticity. GIMIC and NICS were also used to study and confirm the aromaticity of Al_4^{2-} with Li^+ counter ions at the coupled-cluster level.[66] In our work, we calculated the NICS and ring current strength at the same level of theory as above (def2-TZVP/PBE/COSMO). This yields a NICS of −31.8 ppm and net ring current of 27.6 nA/T.

Supplementary Table 3 | Current strength of $[Th@Bi_{12}]^{4-}$ in nA/T at various levels of theory.

Functional	ECP/def(2)-TZVP	DLU-X2C/Jorge-TZP-DKH	DLU-X2C/Dyall-VTZ
BP86	22.4	24.7	23.2
PBE	22.7	24.8	23.4
TPSS	22.9	24.8	23.3
TPSSh	24.0	25.5	24.2

Supplementary Table 4 | Current strength in nA/T and NICS values in ppm of "Bi_{12}^{8-}".

Functional	ECP/def(2)-TZVP		DLU-X2C/Jorge-TZP-DKH		DLU-X2C/Dyall-VTZ	
	Ring Current	NICS	Ring Current	NICS	Ring Current	NICS
BP86	23.4	−16.8	23.0	−15.3	23.3	−17.6
PBE	23.7	−17.1	23.2	−15.4	23.4	−17.8
TPSS	23.4	−17.1	22.8	−15.7	23.1	−17.7
TPSSh	23.7	−17.5	23.0	−16.3	23.4	−18.0

The hypothetical "$[Th@Bi_{12}]^{\pm 0}$" possess a diatropic net ring current of 6.9 nA/T (PBE).

To study the applicability of the 4n+2 rule, we considered the hypothetical "Bi_{12}^{10-}" and "Bi_{12}^{12-}" clusters. For the first, anti-aromaticity would be expected. The closed-shell singlet state is not the electron ground state, the triplet state is lower in energy: 9.76 kJ/mol (BP86), 8.54 kJ/mol (PBE), 8.01 kJ/mol (TPSS), and 9.74 kJ/mol (TPSSh). The triplet ground state is further confirmed by the fractional occupation number approach[67] and optimizing the number of unpaired electrons starting at a high damping level (9 a.u.). In contrast, the closed-shell "Bi_{12}^{12-}" cluster is expected to be aromatic again. This is confirmed by computational studies based on the magnetic criterion. The ring current strength and the NICS values are listed in **Supplementary Table 5.** Here, the cluster sustains a global net ring current of more than 40 nA/T and the NICS about −33 ppm also indicates aromaticity. Furthermore, we calculated the NICS and current strengths of "Bi_{12}^{8-}" and "Bi_{12}^{12-}" with our NMR-tailored x2c-SVPall-s,[28] x2c-TZVPall-s,[28] and x2c-QVZPall-s basis sets[68] and proper auxiliary basis sets[29,68] for the RI-*J* approximation, which are listed in **Supplementary Table 6** and **Supplementary Table 7**, respectively. Here, we also used the B3LYP,[69,70] CAM-B3LYP,[71] and the PBE0[33] hybrid functional.

The optimized structure (Cartesian coordinates) of $[Th@Bi_{12}]^{4-}$ and the four reference compounds (Al_4^{2-}, benzene, porphine, and zinc porphyrin) are listed in a separate file as part of the supplementary material (OptimizedStructures.txt) along with those of all other species shown in **Fig. 3** in the main document and in **Supplementary Figure 16**. The structures of the reference compounds were optimized with grid 3. In addition, **Supplementary Tables 8−12** provide atomic orbital contributions to molecular valence orbitals of all species shown in **Fig. 4** of the main document and in **Supplementary Figure 16**.

Supplementary Table 5 | Current strength in nA/T and NICS values in ppm of "Bi_{12}^{12-}".

Functional	ECP/def(2)-TZVP		DLU-X2C/Jorge-TZP-DKH		DLU-X2C/Dyall-VTZ	
	Ring Current	NICS	Ring Current	NICS	Ring Current	NICS
BP86	42.0	−33.4	41.0	−32.1	41.1	−34.2
PBE	42.9	−34.0	41.8	−32.7	41.9	−34.8
TPSS	42.6	−33.9	41.6	−33.0	41.7	−34.7
TPSSh	42.8	−34.3	41.8	−33.5	41.6	−35.1

Supplementary Table 6 | Current strength in nA/T and NICS values in ppm of "Bi_{12}^{8-}" using the NMR-tailored basis sets and the DLU-X2C Hamiltonian.

Functional	x2c-SVPall-s		x2c-TZVPall-s		x2c-QZVPall-s	
	Ring Current	NICS	Ring Current	NICS	Ring Current	NICS
BP86	21.0	−15.5	21.8	−16.3	23.0	−18.0
B3LYP	20.8	−16.3	21.9	−16.6	23.1	−17.9
CAM-B3LYP	20.2	−16.4	21.4	−16.5	22.8	−17.5
PBE	21.1	−15.6	22.0	−16.5	23.1	−18.2
PBE0	21.2	−16.7	22.3	−17.3	23.6	−18.7
TPSS	20.8	−15.7	21.7	−16.5	22.8	−18.0
TPSSh	20.9	−16.2	21.9	−16.9	23.1	−18.3

Supplementary Table 7 | Current strength in nA/T and NICS values in ppm of "Bi_{12}^{12-}" using the NMR-tailored basis sets and the DLU-X2C Hamiltonian.

Functional	x2c-SVPall-s		x2c-TZVPall-s		x2c-QZVPall-s	
	Ring Current	NICS	Ring Current	NICS	Ring Current	NICS
BP86	36.2	−31.2	37.9	−32.6	40.4	−34.7
B3LYP	35.1	−30.9	36.6	−32.3	38.9	−34.3
CAM-B3LYP	32.3	−29.3	33.7	−30.9	37.0	−33.8
PBE	36.9	−31.7	38.7	−33.2	41.1	−35.2
PBE0	36.7	−32.2	38.7	−33.9	41.0	−36.1
TPSS	36.5	−31.6	38.6	−33.1	40.9	−35.2
TPSSh	36.5	−31.9	38.6	−33.5	40.9	−35.6

6.2. Frontier Orbital Region of the Molecular Orbital (MO) Schemes of Species $[M_x@Bi_{12}]^{q-}$ (M/x/q = La/1/3, U/1/3, Th/1/4

Supplementary Fig. 16 shows all MOs of the valence orbital region of anions based on twelve-atomic bismuth cycles discussed in this work.

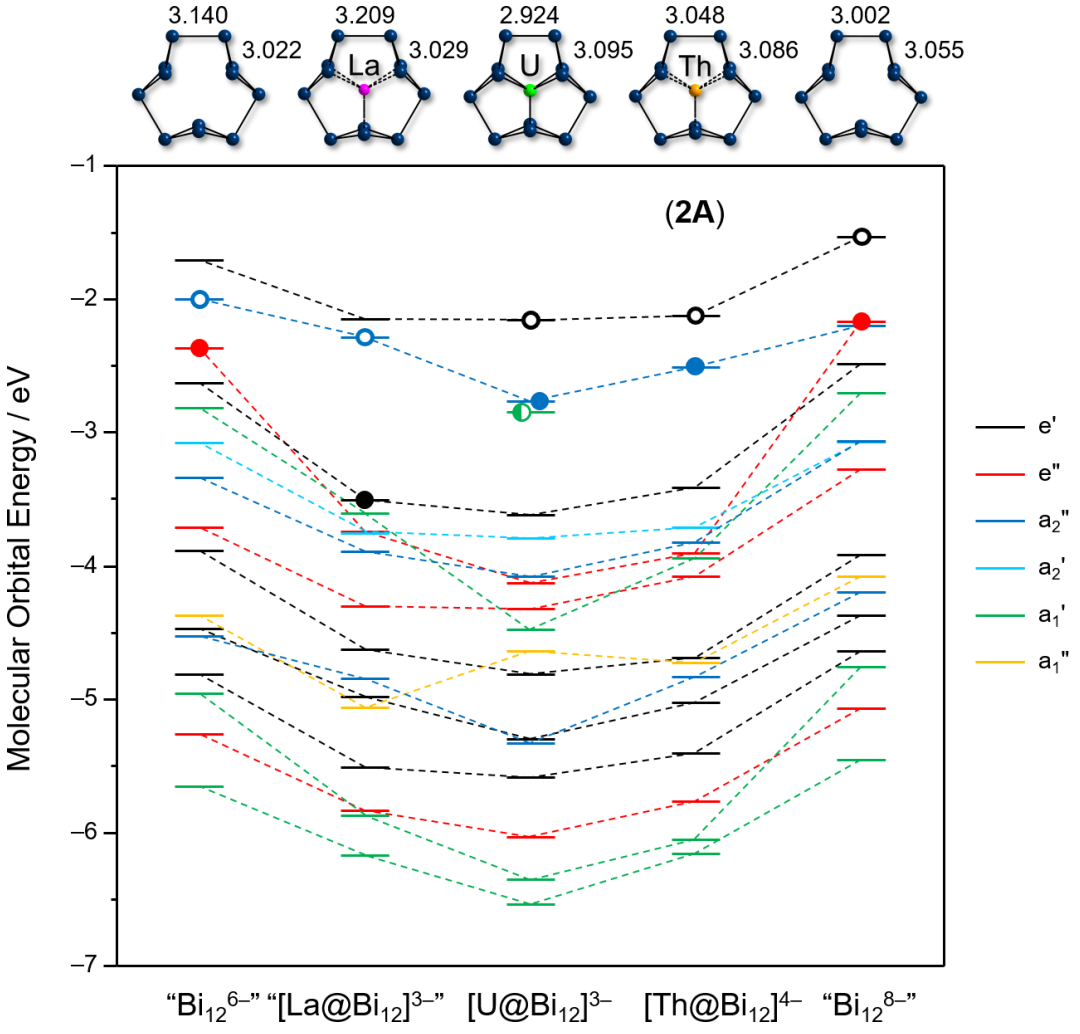

Supplementary Fig. 16 | Frontier orbital region of the molecular orbital (MO) schemes of anions based on 12-atomic polybismuthide rings. All molecules were calculated in D_{3h} symmetry, structural parameters are given in Å. Different irreducible representations are shown in different colours for clarity. A zoom into the scheme, without the six MOs with lowest energies shown here, is provided in **Fig. 4** in the main document. The dashed lines serve as a guide to the eye, thereby denoting changes of corresponding MO energies. The energy of the highest occupied MO (HOMO) is indicated by a filled circle, the lowest unoccupied MO (LUMO) is indicated as an empty circle for each species; the singly occupied f orbital (HOMO−1, a_1') of $[U@Bi_{12}]^{4-}$ is indicated by a half-filled circle. Atomic coordinates and contributions to all valence MOs are given in a separate file as part of the supplementary material and **Supplementary Tables 8−12**.

.

6.3. Atomic Orbital Contributions to Molecular Orbitals

The contributions of atomic orbitals to valence orbitals of the species shown in **Supplementary Fig. 16** and **Fig. 4** of the main document according to Mulliken population analyses[10] are summarized in **Supplementary Tables 8−12**. Note that "ε" denotes the eigenvalue of the Kohn-Sham Fock matrix.

Supplementary Table 8 | Mulliken contributions of atomic orbitals (AOs) to valence molecular orbitals (MOs) of "Bi_{12}^{6-}" (Supplementary Fig. 16 and Fig. 4 in the main document). The atom labelling scheme corresponds with that in **Fig. 2** in the main document.

Mulliken contributions of Bi(A), and Bi(B) to the valence MOs of "Bi_{12}^{6-}" at the ECP/def(2)-TZVP/PBE level using COSMO					
15a1' (ε = −0.2092547 a.u.)					
atom	total	s	p	d	f
Bi(B)	0.17669	0.00044	0.17488	0.00103	0.00033
Bi(A)	0.15665	0.00992	0.14351	0.00294	0.00029
16a1' (ε = −0.1893396 a.u.)					
Bi(B)	0.21675	0.00212	0.21291	0.00157	0.00015
Bi(A)	0.11659	0.00009	0.11332	0.00290	0.00028
17a1' (ε = −0.0969583 a.u.) HOMO					
Bi(B)	0.10781	0.00141	0.09935	0.00638	0.00067
Bi(A)	0.22553	0.00039	0.22346	0.00155	0.00013
11a2' (ε = −0.1246569 a.u.)					
Bi(B)	0.16036	0.00852	0.14633	0.00417	0.00133
Bi(A)	0.17298	0.00000	0.17233	0.00026	0.00039
25e' (ε = −0.1983201 a.u.)					
Bi(B)	0.41905	0.00087	0.41230	0.00522	0.00066
Bi(A)	0.24762	0.00830	0.23128	0.00703	0.00101
26e' (ε = −0.1742786 a.u.)					
Bi(B)	0.43058	0.00654	0.41972	0.00342	0.00090
Bi(A)	0.23609	0.00136	0.22662	0.00729	0.00082
27e' (ε = −0.1490238 a.u.)					
Bi(B)	0.33598	0.01220	0.30659	0.01612	0.00108
Bi(A)	0.33069	0.00061	0.32559	0.00361	0.00088
28e' (ε = −0.1268265 a.u.)					
Bi(B)	0.35465	0.00148	0.33922	0.01255	0.00140
Bi(A)	0.31201	−0.00033	0.30569	0.00556	0.00109
7a1" (ε = −0.1800730 a.u.)					
Bi(B)	0.15508	0.00000	0.15009	0.00463	0.00036
Bi(A)	0.17825	0.00000	0.17712	0.00088	0.00025
11a2" (ε = −0.1559022 a.u.)					
Bi(B)	0.19792	0.00000	0.19445	0.00319	0.00028
Bi(A)	0.13542	0.00609	0.12499	0.00356	0.00077
12a2" (ε = −0.1199662 a.u.)					
Bi(B)	0.01455	0.00000	0.01023	0.00336	0.00096
Bi(A)	0.31879	0.00017	0.31730	0.00117	0.00015
13a2" (ε = −0.0787493 a.u.) LUMO					
Bi(B)	0.13272	0.00000	0.11931	0.01199	0.00142
Bi(A)	0.20061	−0.00594	0.20559	0.00090	0.00006
17e" (ε = −0.1987151 a.u.)					
Bi(B)	0.37471	0.00000	0.37203	0.00220	0.00048
Bi(A)	0.29196	0.00060	0.28812	0.00279	0.00045
18e" (ε = −0.1343181 a.u.)					
Bi(B)	0.25676	0.00000	0.25084	0.00460	0.00132
Bi(A)	0.40990	0.00763	0.39380	0.00695	0.00151
19e" (ε = −0.1063449 a.u.)					
Bi(B)	0.02546	0.00000	0.01494	0.00880	0.00172
Bi(A)	0.64120	0.00068	0.63840	0.00193	0.00019

Supplementary Table 9 | Mulliken contributions of atomic orbitals (AOs) to valence molecular orbitals (MOs) of $[La@Bi_{12}]^{3-}$ (Supplementary Fig. 16 and Fig. 4 in the main document). The atom labelling scheme corresponds with that in **Fig. 2** in the main document.

Mulliken contributions of La, Bi(A), and Bi(B) to the valence MOs of $[La@Bi_{12}]^{3-}$ at the ECP/def(2)-TZVP/PBE level using COSMO					
16a1' (ε = −0.2267385 a.u.)					
atom	total	s	p	d	f
La	0.05661	0.01310	0.00000	0.04046	0.00304
Bi(B)	0.12334	0.00445	0.11441	0.00425	0.00023
Bi(A)	0.20056	0.00064	0.19705	0.00281	0.00006
17a1' (ε = −0.2156283 a.u.)					
La	0.16774	0.14502	0.00000	0.02269	0.00002
Bi(B)	0.13079	0.00351	0.12423	0.00278	0.00028
Bi(A)	0.17459	0.00422	0.16631	0.00397	0.00009
18a1' (ε = −0.1324037 a.u.)					
La	0.32145	0.05091	0.00000	0.26841	0.00213
Bi(B)	0.17350	0.00054	0.16917	0.00327	0.00053
Bi(A)	0.10626	0.00209	0.10273	0.00081	0.00062
11a2' (ε = −0.1374637 a.u.)					
La	0.01230	0.00000	0.00000	0.00000	0.01230
Bi(B)	0.13253	0.00000	0.13022	0.00145	0.00086
Bi(A)	0.19875	0.00474	0.19083	0.00210	0.00108
26e' (ε = −0.2025036 a.u.)					
La	0.26859	0.00000	0.00496	0.26224	0.00138
Bi(B)	0.24884	0.01253	0.22650	0.00890	0.00091
Bi(A)	0.37307	0.01178	0.35273	0.00799	0.00056
27e' (ε = −0.1831528 a.u.)					
La	0.01993	0.00000	−0.02646	0.04603	0.00036
Bi(B)	0.15330	0.00077	0.14377	0.00753	0.00123
Bi(A)	0.51005	0.01027	0.49521	0.00420	0.00037
28e' (ε = −0.1700300 a.u.)					
La	0.28522	0.00000	0.00804	0.27718	0.00000
Bi(B)	0.21932	0.00026	0.21234	0.00530	0.00143
Bi(A)	0.39981	0.00456	0.38398	0.00957	0.00170
29e' (ε = −0.1289576 a.u.) HOMO					
La	0.19551	0.00000	0.00731	0.17646	0.01174
Bi(B)	0.38431	0.00054	0.37879	0.00375	0.00123
Bi(A)	0.24977	0.00520	0.22794	0.01430	0.00233
7a1" (ε = −0.1861400 a.u.)					
Bi(B)	0.16865	0.00000	0.16406	0.00428	0.00032
Bi(A)	0.16468	0.00000	0.16225	0.00189	0.00055
12a2" (ε = −0.1780877 a.u.)					
La	0.03678	0.00000	0.03337	0.00000	0.00341
Bi(B)	0.18282	0.00559	0.17503	0.00171	0.00048
Bi(A)	0.14438	0.00000	0.14331	0.00058	0.00050
13a2" (ε = −0.1432524 a.u.)					
La	−0.01445	0.00000	−0.01581	0.00000	0.00136
Bi(B)	0.30938	0.00172	0.30721	0.00028	0.00017
Bi(A)	0.02636	0.00000	0.01832	0.00722	0.00082
14a2" (ε = −0.0838910 a.u.) LUMO					
La	−0.05074	0.00000	−0.05269	0.00000	0.00195
Bi(B)	0.15299	−0.00771	0.15698	0.00342	0.00030
Bi(A)	0.18880	0.00000	0.17510	0.01218	0.00152
17e" (ε = −0.2144991 a.u.)					
La	0.16003	0.00000	0.00000	0.15585	0.00419
Bi(B)	0.30900	0.00140	0.30315	0.00425	0.00020
Bi(A)	0.33100	0.00000	0.32560	0.00519	0.00021
18e" (ε = −0.1580887 a.u.)					
La	0.03476	0.00000	0.00000	0.03217	0.00259
Bi(B)	0.40216	0.01569	0.38357	0.00180	0.00110
Bi(A)	0.25871	0.00000	0.25175	0.00562	0.00135
19e" (ε = −0.1376712 a.u.)					
La	0.72791	0.00000	0.00000	0.71663	0.01128
Bi(B)	0.48439	0.00037	0.47859	0.00457	0.00086
Bi(A)	0.06096	0.00000	0.05110	0.00763	0.00223

Supplementary Table 10 | Mulliken contributions of atomic orbitals (AOs) to valence molecular orbitals (MOs) of $[U@Bi_{12}]^{4-}$ (Supplementary Fig. 16 and Fig. 4 in the main document). The atom labelling scheme corresponds with that in **Fig. 2** in the main document.

Mulliken contributions of U, Bi(A), and Bi(B) to the valence MOs of $[U@Bi_{12}]^{4-}$ at the ECP/def(2)-TZVP/PBE level using COSMO					
16a1' α (ε = −0.2397690 a.u.)					
atom	total	s	p	d	f
U	0.07663	0.00217	0.00000	0.07135	0.00311
Bi(B)	0.06633	0.00068	0.06355	0.00203	0.00007
Bi(A)	0.08757	0.00019	0.08613	0.00121	0.00004
17a1' α (ε = −0.2324428 a.u.)					
U	0.08697	0.08490	0.00000	0.00202	0.00006
Bi(B)	0.07925	0.00403	0.07361	0.00155	0.00005
Bi(A)	0.07292	0.00225	0.06756	0.00302	0.00010
18a1' α (ε = −0.1631745 a.u.)					
U	0.19740	0.02305	0.00000	0.16861	0.00573
Bi(B)	0.06008	0.00159	0.05575	0.00222	0.00052
Bi(A)	0.07368	0.00243	0.07069	0.00031	0.00026
11a2' α (ε = −0.1392247 a.u.)					
U	0.07656	0.00000	0.00000	0.00000	0.07656
Bi(B)	0.05448	0.00000	0.05251	0.00137	0.00060
Bi(A)	0.09943	0.00186	0.09721	−0.00016	0.00052
26e' α (ε = −0.2045006 a.u.)					
U	0.25341	0.00000	0.00005	0.25017	0.00319
Bi(B)	0.09549	0.00360	0.08608	0.00529	0.00052
Bi(A)	0.19561	0.01017	0.18180	0.00332	0.00032
27e' α (ε = −0.1942777 a.u.)					
U	0.05164	0.00000	0.02710	0.02073	0.00381
Bi(B)	0.11032	0.00291	0.10383	0.00297	0.00062
Bi(A)	0.21440	0.00426	0.20547	0.00430	0.00037
28e' α (ε = −0.1762217 a.u.)					
U	0.10593	0.00000	0.00656	0.09833	0.00104
Bi(B)	0.08752	0.00064	0.08343	0.00272	0.00073
Bi(A)	0.22816	0.00324	0.22005	0.00397	0.00089
29e' α (ε = −0.1309009 a.u.)					
U	0.28890	0.00000	−0.00030	0.10707	0.18213
Bi(B)	0.22197	−0.00132	0.22107	0.00135	0.00087
Bi(A)	0.06322	−0.00053	0.05781	0.00479	0.00114
30e' α (ε = −0.0794484 a.u.) LUMO (α spin)					
Bi(B)	0.19658	−0.00185	0.19238	0.00487	0.00118
Bi(A)	0.13651	−0.00751	0.13374	0.00967	0.00061
7a1" α (ε = −0.1708066 a.u.)					
Bi(B)	0.08181	0.00000	0.07855	0.00308	0.00017
Bi(A)	0.08486	0.00000	0.08342	0.00109	0.00035
12a2" α (ε = −0.1959519 a.u.)					
U	0.01748	0.00000	0.00356	0.00000	0.01392
Bi(B)	0.10264	0.00096	0.09982	0.00166	0.00020
Bi(A)	0.06111	0.00000	0.06060	0.00027	0.00024
13a2" α (ε = −0.1500130 a.u.)					
U	0.02367	0.00000	0.01757	0.00000	0.00610
Bi(B)	0.14236	0.00212	0.13990	0.00016	0.00017
Bi(A)	0.02036	0.00000	0.01686	0.00309	0.00040
14a2" α (ε = −0.1005623 a.u.) HOMO (α spin)					
U	0.04634	0.00000	−0.00089	0.00000	0.04723
Bi(B)	0.06815	−0.00466	0.07014	0.00243	0.00024
Bi(A)	0.09079	0.00000	0.08348	0.00654	0.00078
17e" α (ε = −0.2219263 a.u.)					
U	0.18025	0.00000	0.00000	0.16790	0.01234
Bi(B)	0.15548	0.00205	0.15132	0.00206	0.00004
Bi(A)	0.14781	0.00000	0.14387	0.00373	0.00021
18e" α (ε = −0.1576063 a.u.)					
U	0.36239	0.00000	0.00000	0.29502	0.06737
Bi(B)	0.23172	0.00516	0.22598	0.00009	0.00049
Bi(A)	0.04122	0.00000	0.03814	0.00203	0.00105

Supplementary Table 10 (continued).

19e" α (ε = −0.1517349 a.u.)					
U	0.19637	0.00000	0.00000	0.18698	0.00939
Bi(B)	0.16023	0.00144	0.15254	0.00515	0.00110
Bi(A)	0.14037	0.00000	0.13659	0.00314	0.00064
16a1' α (ε = −0.2408002 a.u.)					
U	0.09244	0.00349	0.00000	0.08190	0.00704
Bi(B)	0.06576	0.00113	0.06235	0.00219	0.00008
Bi(A)	0.08550	0.00033	0.08387	0.00125	0.00005
17a1' α (ε = −0.2345978 a.u.)					
U	0.10733	0.10644	0.00000	0.00052	0.00037
Bi(B)	0.07671	0.00395	0.07123	0.00148	0.00005
Bi(A)	0.07207	0.00213	0.06681	0.00302	0.00010
18a1' β (ε = −0.1662159 a.u.)					
U	0.23659	0.02036	0.00000	0.19025	0.02598
Bi(B)	0.05690	0.00181	0.05271	0.00186	0.00052
Bi(A)	0.07033	0.00246	0.06731	0.00032	0.00024
19a1' β (ε = −0.1047625 a.u.)					
U	0.81238	0.01875	0.00000	0.00233	0.79130
Bi(A)	0.02339	0.00010	0.01917	0.00346	0.00066
11a2' β (ε = −0.1393655 a.u.)					
U	0.08969	0.00000	0.00000	0.00000	0.08969
Bi(B)	0.05282	0.00000	0.05082	0.00139	0.00061
Bi(A)	0.09890	0.00183	0.09679	−0.00022	0.00050
26e' β (ε = −0.2060103 a.u.)					
U	0.32244	0.00000	−0.00001	0.31890	0.00355
Bi(B)	0.09196	0.00363	0.08273	0.00505	0.00055
Bi(A)	0.18763	0.01063	0.17356	0.00311	0.00033
27e' β (ε = −0.1950749 a.u.)					
U	0.05746	0.00000	0.03392	0.02099	0.00255
Bi(B)	0.11115	0.00331	0.10426	0.00296	0.00062
Bi(A)	0.21261	0.00377	0.20377	0.00468	0.00039
28e' β (ε = −0.1772401 a.u.)					
U	0.11943	0.00000	0.00944	0.10981	0.00018
Bi(B)	0.08172	0.00064	0.07745	0.00288	0.00074
Bi(A)	0.23171	0.00327	0.22366	0.00390	0.00087
29e' β (ε = −0.1351328 a.u.)					
U	0.42730	0.00000	−0.00175	0.10548	0.32356
Bi(B)	0.20595	−0.00151	0.20552	0.00106	0.00089
Bi(A)	0.05616	−0.00032	0.05119	0.00426	0.00103
30e' β (ε = −0.0790651 a.u.) LUMO (β spin)					
Bi(B)	0.20199	−0.00223	0.19840	0.00468	0.00115
Bi(A)	0.13019	−0.00704	0.12735	0.00928	0.00060
7a1" β (ε = −0.1701161 a.u.)					
Bi(B)	0.08130	0.00000	0.07807	0.00307	0.00017
Bi(A)	0.08537	0.00000	0.08392	0.00109	0.00035
12a2" β (ε = −0.1958129 a.u.)					
U	0.02505	0.00000	0.00393	0.00000	0.02112
Bi(B)	0.10162	0.00096	0.09865	0.00180	0.00021
Bi(A)	0.06087	0.00000	0.06036	0.00027	0.00025
13a2" β (ε = −0.1500959 a.u.)					
U	0.03059	0.00000	0.02043	0.00000	0.01016
Bi(B)	0.14239	0.00221	0.13996	0.00007	0.00015
Bi(A)	0.01918	0.00000	0.01566	0.00311	0.00041
14a2" β (ε = −0.1025496 a.u.) (β spin)					
U	0.14408	0.00000	−0.00105	0.00000	0.14513
Bi(B)	0.05485	−0.00425	0.05604	0.00267	0.00039
Bi(A)	0.08781	0.00000	0.08104	0.00606	0.00071
17e" β (ε = −0.2217470 a.u.)					
U	0.19947	0.00000	0.00000	0.18424	0.01523
Bi(B)	0.15316	0.00219	0.14890	0.00204	0.00004
Bi(A)	0.14693	0.00000	0.14297	0.00375	0.00021
18e" β (ε = −0.1599441 a.u.)					
U	0.50703	0.00000	0.00000	0.39671	0.11032
Bi(B)	0.22409	0.00354	0.21901	0.00092	0.00062
Bi(A)	0.02474	0.00000	0.02202	0.00170	0.00103

Supplementary Table 10 (continued).

19e" β (ε = −0.1517744 a.u.)					
U	0.10094	0.00000	0.00000	0.09876	0.00218
Bi(B)	0.15876	0.00303	0.15032	0.00441	0.00101
Bi(A)	0.15775	0.00000	0.15380	0.00333	0.00062

Supplementary Table 11 | Mulliken contributions of atomic orbitals (AOs) to valence molecular orbitals (MOs) of $[Th@Bi_{12}]^{4-}$ (Supplementary Fig. 16 and Fig. 4 in the main document). The atom labelling scheme corresponds with that in **Fig. 2** in the main document.

Mulliken contributions of Th, Bi(A), and Bi(B) to the valence MOs of $[Th@Bi_{12}]^{4-}$ at the ECP/def(2)-TZVP/PBE level using COSMO					
16a1' (ε = −0.2263257 a.u.)					
atom	total	s	p	d	f
Th	0.11326	0.01674	0.00000	0.09063	0.00585
Bi(B)	0.13357	0.00457	0.12481	0.00403	0.00016
Bi(A)	0.18089	0.00056	0.17766	0.00256	0.00011
17a1' (ε = −0.2223264 a.u.)					
Th	0.21972	0.21299	0.00000	0.00653	0.00020
Bi(B)	0.13507	0.00423	0.12816	0.00251	0.00017
Bi(A)	0.16164	0.00411	0.15282	0.00458	0.00013
18a1' (ε = −0.1449244 a.u.)					
Th	0.40042	0.06606	0.00000	0.32621	0.00788
Bi(B)	0.14210	0.00144	0.13653	0.00339	0.00075
Bi(A)	0.12449	0.00309	0.12021	0.00063	0.00057
11a2' (ε = −0.1364050 a.u.)					
Th	0.04784	0.00000	0.00000	0.00000	0.04784
Bi(B)	0.12266	0.00000	0.11975	0.00197	0.00094
Bi(A)	0.20269	0.00435	0.19668	0.00069	0.00098
26e' (ε = −0.1985834 a.u.)					
Th	0.41579	0.00000	0.00459	0.40757	0.00325
Bi(B)	0.22110	0.01062	0.20075	0.00882	0.00090
Bi(A)	0.37627	0.01293	0.35614	0.00660	0.00060
27e' (ε = −0.1846237 a.u.)					
Th	0.16342	0.00000	0.05896	0.10264	0.00166
Bi(B)	0.17503	0.00226	0.16680	0.00480	0.00117
Bi(A)	0.46440	0.01157	0.44634	0.00600	0.00049
28e' (ε = −0.1723174 a.u.)					
Th	0.25737	0.00000	0.01335	0.24276	0.00011
Bi(B)	0.18915	0.00142	0.18052	0.00587	0.00135
Bi(A)	0.43462	0.00411	0.42159	0.00738	0.00155
29e' (ε = −0.1253780 a.u.)					
Th	0.27128	0.00000	0.00875	0.19529	0.06720
Bi(B)	0.44999	−0.00083	0.44707	0.00267	0.00108
Bi(A)	0.17146	0.00216	0.15498	0.01205	0.00228
30e' (ε = −0.0779870 a.u.) LUMO					
Th	−0.01413	0.00000	0.00250	−0.02220	0.00332
Bi(B)	0.41541	−0.00216	0.40475	0.01064	0.00218
Bi(A)	0.25361	−0.01461	0.24957	0.01745	0.00121
7a1" (ε = −0.1737260 a.u.)					
Bi(B)	0.16637	0.00000	0.16185	0.00425	0.00027
Bi(A)	0.16674	0.00000	0.16389	0.00227	0.00058
12a2" (ε = −0.1774834 a.u.)					
Th	0.02484	0.00000	0.01377	0.00000	0.01107
Bi(B)	0.18850	0.00384	0.18203	0.00220	0.00044
Bi(A)	0.14069	0.00000	0.13989	0.00030	0.00050
13a2" (ε = −0.1404908 a.u.)					
Th	0.05272	0.00000	0.04862	0.00000	0.00400
Bi(B)	0.29026	0.00215	0.28755	0.00032	0.00024
Bi(A)	0.03428	0.00000	0.02702	0.00654	0.00072
14a2" (ε = −0.0920928 a.u.) HOMO					
Th	0.01848	0.00000	0.00386	0.00000	0.01325
Bi(B)	0.15803	−0.00976	0.16380	0.00374	0.00025
Bi(A)	0.17223	0.00000	0.15824	0.01252	0.00148

Supplementary Table 11 (continued).

17e" (ε = −0.2120068 a.u.)					
Th	0.25551	0.00000	0.00000	0.24388	0.01153
Bi(B)	0.30474	0.00232	0.29867	0.00366	0.00009
Bi(A)	0.31934	0.00000	0.31289	0.00618	0.00027
18e" (ε = −0.1498338 a.u.)					
Th	0.24530	0.00000	0.00000	0.21767	0.02618
Bi(B)	0.43935	0.01286	0.42497	0.00067	0.00086
Bi(A)	0.18643	0.00000	0.17967	0.00499	0.00178
19e" (ε = −0.1434746 a.u.)					
Th	0.71197	0.00000	0.00000	0.68587	0.02558
Bi(B)	0.38907	0.00064	0.38001	0.00694	0.00148
Bi(A)	0.15894	0.00000	0.15160	0.00585	0.00149

Supplementary Table 12 | Mulliken contributions of atomic orbitals (AOs) to valence molecular orbitals (MOs) of "Bi_{12}^{8-}" (Supplementary Fig. 16 and Fig. 4 in the main document). The atom labelling scheme corresponds with that in **Fig. 2** in the main document.

Mulliken contributions of Bi(A) and Bi(B) to the valence MOs of Bi_{12}^{8-} at the ECP/def(2)-TZVP/PBE level using COSMO					
15a1' (ε = −0.2004016 a.u.)					
atom	total	s	p	d	f
Bi(B)	0.19462	0.00003	0.19339	0.00112	0.00008
Bi(A)	0.13871	0.00357	0.13342	0.00156	0.00017
16a1' (ε = −0.1749722 a.u.)					
Bi(B)	0.18776	0.00225	0.18264	0.00275	0.00011
Bi(A)	0.14558	−0.00046	0.14712	−0.00130	0.00021
17a1' (ε = −0.0992400 a.u.)					
Bi(B)	0.11237	0.00280	0.10408	0.00450	0.00099
Bi(A)	0.22096	−0.00028	0.21973	0.00144	0.00007
11a2' (ε = −0.1129345 a.u.)					
Bi(B)	0.21023	0.00321	0.20293	0.00298	0.00112
Bi(A)	0.12310	0.00000	0.12073	0.00153	0.00084
25e' (ε = −0.1705667 a.u.)					
Bi(B)	0.42599	0.00300	0.41549	0.00691	0.00058
Bi(A)	0.24068	0.00826	0.22499	0.00657	0.00087
26e' (ε = −0.1607234 a.u.)					
Bi(B)	0.51719	0.00939	0.50628	0.00106	0.00045
Bi(A)	0.14948	−0.00007	0.14611	0.00254	0.00090
27e' (ε = −0.1439596 a.u.)					
Bi(B)	0.35455	0.00652	0.33621	0.01015	0.00166
Bi(A)	0.31212	0.00160	0.30853	0.00099	0.00100
28e' (ε = −0.0913007 a.u.)					
Bi(B)	0.27122	−0.00154	0.26034	0.01048	0.00194
Bi(A)	0.39545	0.00060	0.38643	0.00725	0.00118
29e' (ε = −0.0563593 a.u.) LUMO					
Bi(B)	0.24318	−0.02551	0.25303	0.01461	0.00105
Bi(A)	0.42349	−0.00219	0.40795	0.01584	0.00188
7a1" (ε = −0.1500247 a.u.)					
Bi(B)	0.17600	0.00000	0.17287	0.00247	0.00066
Bi(A)	0.15733	0.00000	0.15251	0.00452	0.00031
11a2" (ε = −0.1541818 a.u.)					
Bi(B)	0.14442	0.00000	0.14373	0.00014	0.00055
Bi(A)	0.18891	0.00333	0.18361	0.00151	0.00047
12a2" (ε = −0.1125620 a.u.)					
Bi(B)	0.04967	0.00000	0.04327	0.00582	0.00058
Bi(A)	0.28366	−0.00109	0.28143	0.00295	0.00036
13a2" (ε = −0.0810022 a.u.)					
Bi(B)	0.15102	0.00000	0.13891	0.01075	0.00136
Bi(A)	0.18232	−0.00709	0.18784	0.00148	0.00008
17e" (ε = −0.1863270 a.u.)					
Bi(B)	0.36827	0.00000	0.36361	0.00440	0.00026
Bi(A)	0.29840	0.00110	0.29496	0.00191	0.00042

Supplementary Table 12 (continued).

18e" (ε = −0.1202864 a.u.)					
Bi(B)	0.32469	0.00000	0.31732	0.00625	0.00112
Bi(A)	0.34198	0.01114	0.32224	0.00704	0.00156
19e" (ε = −0.0796599 a.u.) HOMO					
Bi(B)	0.02733	0.00000	0.01920	0.00594	0.00219
Bi(A)	0.63934	−0.00063	0.63386	0.00582	0.00029

7. References for the Supplementary Information

1. Xu, L. & Sevov, S. C. Heteroatomic Deltahedral Clusters of Main-Group Elements: Synthesis and Structure of the Zintl Ions $[In_4Bi_5]^{3-}$, $[InBi_3]^{2-}$, and $[GaBi_3]^{2-}$. *Inorg. Chem.* **39,** 5383-5389 (2000).
2. Cisar, A. & Corbett, J. D. Polybismuth anions. Synthesis and crystal structure of a salt of the tetrabismuthide(2−) ion, Bi_4^{2-}. A basis for the interpretation of the structure of some complex intermetallic phases. *Inorg. Chem.* **16,** 2482-2487 (1977).
3. Deubner, H. L., Rudel, S. S. & Kraus, F. A Simple Access to Pure Thorium(IV) Halides ($ThCl_4$, $ThBr_4$ & ThI_4). *Z. Anorg. Allg. Chem.* **643,** 2005-2010 (2017).
4. Lichtenberger, N., Spang, N., Eichhöfer, A. & Dehnen, S. Between Localization and Delocalization: $Ru(cod)^{2+}$ Units in the Zintl Clusters $[Bi_9\{Ru(cod)\}_2]^{3-}$ and $[Tl_2Bi_6\{Ru(cod)\}]^{2-}$. *Angew. Chem. Int. Ed.* **56,** 13253-13258 (2017).
5. Ababei, R. et al. Making practical use of the pseudo-element concept: an efficient way to ternary intermetalloid clusters by an isoelectronic Pb^-–Bi combination. *Chem. Commun.* **48,** 11295-11297 (2012).
6. Lichtenberger, N. et al. Main Group Metal–Actinide Magnetic Coupling and Structural Response Upon U^{4+} Inclusion Into Bi, Tl/Bi, or Pb/Bi Cages. *J. Am. Chem. Soc.* **138,** 9033-9036 (2016).
7. Mitzinger, S., Broeckaert, L., Massa, W., Weigend, F. & Dehnen, S. Understanding of multimetallic cluster growth. *Nat. Commun.* **7,** 10480-10490 (2016).
8. Lips, F. et al. Doped Semimetal Clusters: Ternary, Intermetalloid Anions $[Ln@Sn_7Bi_7]^{4-}$ and $[Ln@Sn_4Bi_9]^{4-}$ (Ln = La, Ce) with Adjustable Magnetic Properties. *J. Am. Chem. Soc.* **134,** 1181-1191 (2012).
9. Dolomanov, O. V., Bourhis, L. J., Gildea, R. J., Howard, J. A. K. & Puschmann, H. OLEX2: a complete structure solution, refinement and analysis program. *J. Appl. Cryst*. **42,** 339-341 (2009).
10. TURBOMOLE, Version 7.4.1 2019 and Version 7.5 2020, a development of University of Karlsruhe and Forschungszentrum Karlsruhe GmbH 1989-2007, TURBOMOLE GmbH since 2007, available via https://www.turbomole.org (retrieved January 30, 2020).
11. Ahlrichs, R., Bär, M., Häser, M., Horn, H. & Kölmel, C. Electronic structure calculations on workstation computers: The program system turbomole. *Chem. Phys. Lett*. **162,** 165-169 (1989).
12. Furche, F., Ahlrichs, R., Hättig, C., Klopper, W., Sierka, M. & Weigend, F. Turbomole. *Wiley Interdiscip. Rev.: Comput. Mol. Sci.* **4,** 91-100 (2014).
13. Balasubramani, S. G. et al. TURBOMOLE: Modular program suite for *ab initio* quantum-chemical and condensed-matter simulations. *J. Chem. Phys.* **152,** 184107 (2020).
14. Perdew, J. P., Burke, K. & Ernzerhof, M. Generalized Gradient Approximation Made Simple. *Phys. Rev. Lett.* **77,** 3865–868 (1996). Erratum: *Phys. Rev. Lett.* **78,** 1396 (1997).
15. Weigend, F. & Ahlrichs, R. Balanced basis sets of split valence, triple zeta valence and quadruple zeta valence quality for H to Rn: Design and assessment of accuracy. *Phys. Chem. Chem. Phys*. **7,** 3297-3305 (2005).
16. Weigend, F. Accurate Coulomb-fitting basis sets for H to Rn. *Phys. Chem. Chem. Phys.* **8,** 1057-1065 (2006).
17. Treutler, O. & Ahlrichs, R. Efficient molecular numerical integration schemes. *J. Chem. Phys*. **102,** 346-354 (1995).
18. Klamt, A. & Schüürmann, G. COSMO: a new approach to dielectric screening in solvents with explicit expressions for the screening energy and its gradient. *J. Chem. Soc., Perkin Trans. 2*, 799-805 (1993).
19. Schäfer, A., Klamt, A., Sattel, D., Lohrenz, J. C. W. & Eckert, F. COSMO Implementation in TURBOMOLE: Extension of an efficient quantum chemical code towards liquid systems. *Phys. Chem. Chem. Phys*. **2,** 2187-2193 (2000).

20. Grimme, S., Antony, J., Ehrlich, S. & Krieg, H. A consistent and accurate ab initio parametrization of density functional dispersion correction (DFT-D) for the 94 elements H-Pu. *J. Chem. Phys*. **132,** 154104 (2010).
21. Caldeweyher, E., Bannwarth, C. & Grimme, S. Extension of the D3 dispersion coefficient model. *J. Chem. Phys*. **147,** 034112 (2017).
22. Caldeweyher, E., Ehlert, S., Hansen, A., Neugebauer, H., Spicher, S., Bannwarth, C. & Grimme, S. A generally applicable atomic-charge dependent London dispersion correction. *J. Chem. Phys*. **150,** 154112 (2019).
23. Peng, D., Middendorf, N., Weigend, F. & Reiher, M. An efficient implementation of two-component relativistic exact-decoupling methods for large molecules. *J. Chem. Phys.* **138,** 184105 (2013).
24. Franzke, Y. J., Middendorf, N. & Weigend, F. Efficient implementation of one- and two-component analytical energy gradients in exact two-component theory. *J. Chem. Phys.* **148,** 104110 (2018).
25. Franzke, Y. J. & Weigend, F. NMR Shielding Tensors and Chemical Shifts in Scalar-Relativistic Local Exact Two-Component Theory. *J. Chem. Theory Comput.* **15,** 1028-1043 (2019).
26. Peng, D. & Reiher, M. Local relativistic exact decoupling. *J. Chem. Phys.* **136,** 244108 (2012).
27. Visscher, L. & Dyall, K. G. DIRAC–FOCK ATOMIC ELECTRONIC STRUCTURE CALCULATIONS USING DIFFERENT NUCLEAR CHARGE DISTRIBUTIONS. *At. Data Nucl. Data Tables* **67,** 207-224 (1997).
28. Franzke, Y. J., Treß, R., Pazdera, T. M. & Weigend, F. Error-consistent segmented contracted all-electron relativistic basis sets of double- and triple-zeta quality for NMR shielding constants. *Phys. Chem. Chem. Phys*. **21,** 16658-16664 (2019).
29. Pollak, P. & Weigend, F. Segmented Contracted Error-Consistent Basis Sets of Double- and Triple-ζ Valence Quality for One- and Two-Component Relativistic All-Electron Calculations. *J. Chem. Theory Comput.* **13,** 3696-3705 (2017).
30. Metz, B., Stoll, H. & Dolg, M. Small-core multiconfiguration-Dirac–Hartree–Fock-adjusted pseudopotentials for post-d main group elements: Application to PbH and PbO. *J. Chem. Phys.* **113,** 2563-2569 (2000).
31. Andrae, D., Häußermann, U., Dolg, M., Stoll, H. & Preuss, H. Energy-adjusted ab initio pseudopotentials for the second and third row transition elements. *Theor. Chim. Acta* **77,** 123 (1990).
32. Reiter, K., Mack, F. & Weigend, F. Calculation of Magnetic Shielding Constants with meta-GGA Functionals Employing the Multipole-Accelerated Resolution of the Identity: Implementation and Assessment of Accuracy and Efficiency. *J. Chem. Theory Comput.* **14,** 191-197 (2018).
33. Adamo, C. & Barone, V. Toward chemical accuracy in the computation of NMR shieldings: the PBE0 model. *Chem. Phys. Lett.* **297,** 113-119 (1998).
34. Rappoport, D. & Furche, F. Property-optimized Gaussian basis sets for molecular response calculations. *J. Chem. Phys*. **133,** 134105 (2010).
35. Schleyer, P., Maerker, C. Dransfeld, A. Jiao, H. & Hommes, N. Nucleus-independent Chemical Shifts: A Simple and Efficient Aromaticity Probe. *J. Am. Chem. Soc*. **118,** 6317-6318 (1996).
36. Jiménez-Halla, J. O. C., Matito, E., Robles, J. & Solà, M. Nucleus-independent chemical shift (NICS) profiles in a series of monocyclic planar inorganic compounds. *J. Organomet. Chem*. **691,** 4359-4366 (2006).
37. Cao, X., Dolg, M. & Stoll, H. Valence basis sets for relativistic energy-consistent small-core actinide pseudopotentials. *J. Chem. Phys*. **118,** 487-496 (2003).
38. Bauernschmitt, R. & Ahlrichs, R. Treatment of electronic excitations within the adiabatic approximation of time dependent density functional theory. *Chem. Phys. Lett.* **256,** 454-464 (1996).
39. Bauernschmitt, R., Häser, M., Treutler, O. & Ahlrichs, R. Calculation of excitation energies within time-dependent density functional theory using auxiliary basis set expansions. *Chem. Phys. Lett*. **264,** 573-578 (1997).

40. Furche, F. & Rappoport, D. Density functional theory for excited states: equilibrium structure and electronic spectra. In *Computational Photochemistry* (ed. Olivucci, M.), p. 93-128 (Elsevier, Amsterdam, 2005).
41. Boys, S. F. Construction of Some Molecular Orbitals to Be Approximately Invariant for Changes from One Molecule to Another. *Rev. Mod. Phys*. **32,** 296-299 (1960).
42. Knizia, G. Intrinsic Atomic Orbitals: An Unbiased Bridge between Quantum Theory and Chemical Concepts. *J. Chem. Theory Comput*. **9,** 4834-4843 (2013).
43. Mulliken, R. S. Electronic Population Analysis on LCAO–MO Molecular Wave Functions. I. *J. Chem. Phys*. **23,** 1833-1840 (1955).
44. Becke, A. D. & Edgecombe, K. E. A simple measure of electron localization in atomic and molecular systems. *J. Chem. Phys*. **92,** 5397–5403 (1990).
45. Becke, A. D. Density-functional exchange-energy approximation with correct asymptotic behavior. *Phys. Rev. A: At., Mol., Opt. Phys.* **38,** 3098–3100 (1988).
46. Perdew, J. P. Density-functional approximation for the correlation energy of the inhomogeneous electron gas. *Phys. Rev. B: Condens. Matter Mater. Phys*. **33,** 8822–8824 (1986). Erratum: *Phys. Rev. B* **34,** 7406 (1986).
47. Tao, J., Perdew, J. P., Staroverov, V. N. & Scuseria, G. E. Climbing the Density Functional Ladder: Nonempirical Meta–Generalized Gradient Approximation Designed for Molecules and Solids. *Phys. Rev. Lett*. **93,** 146401 (2003).
48. Staroverov, V. N., Scuseria, G. E., Tao, J. & Perdew, J. P. Comparative assessment of a new nonempirical density functional: Molecules and hydrogen-bonded complexes. *J. Chem. Phys*. **119,** 12129–12137 (2003). Erratum: *J. Chem. Phys.* **121,** 11507 (2003).
49. Martins, L. S. C., Jorge, F. E. & Machado, S. F. All-electron segmented contraction basis sets of triple zeta valence quality for the fifth-row elements. *Mol. Phys.* **113,** 3578-3586 (2015).
50. Oliveira, A. Z., Campos, C. T., Jorge, F. E., Ferreira, I. B. & Fantin, P. All-electron triple zeta basis sets for the actinides. *Comput. Theor. Chem*. **1135,** 28-33 (2018).
51. Pritchard, B. P., Altarawy, D., Didier, B., Gibson, T. D. & Windus, T. L. New Basis Set Exchange: An Open, Up-to-Date Resource for the Molecular Sciences Community. *J. Chem. Inf. Model.* **59,** 4814-4820 (2019).
52. Basis Set Exchange ver2, BSE Library v0.8.12, https://www.basissetexchange.org/ (retrieved May 12, 2020).
53. Dyall, K. G. Relativistic and nonrelativistic finite nucleus optimized triple-zeta basis sets for the 4p, 5p and 6p elements. *Theor. Chem. Acc.* **108,** 335-340 (2002). Erratum: *Theor. Chem. Acc.* **109,** 284 (2003).
54. Dyall, K. G. Relativistic Quadruple-Zeta and Revised Triple-Zeta and Double-Zeta Basis Sets for the 4p, 5p, and 6p Elements. *Theor. Chem. Acc.* **115,** 441-447 (2006).
55. Dyall, K. G. Relativistic double-zeta, triple-zeta, and quadruple-zeta basis sets for the actinides Ac–Lr. *Theor. Chem. Acc.* **117,** 491-500 (2007).
56. Basis sets are available from the Dirac program web site, http://dirac.chem.sdu.dk (retrieved December 25, 2019). Note that we have deleted the inner-most g-function from the 6d/7s correlating set of Th to remove linear dependencies.
57. Jusélius, J., Sundholm, D. & Gauss, J. Calculation of current densities using gauge-including atomic orbitals. *J. Chem. Phys.* **121,** 3952-3963 (2004).
58. GIMIC Version 2.1.4 (3a5f0eb) 2019, available via https://github.com/qmcurrents/gimic (retrieved January 30, 2020).
59. Fliegl, H., Taubert, S., Lehtonen, O. & Sundholm, D. The gauge including magnetically induced current method. *Phys. Chem. Chem. Phys.* **13,** 20500-20518 (2011).
60. Sundholm, D., Fliegl, H. & Berger, R. J. Calculations of magnetically induced current densities: theory and applications. *Wiley Interdiscip. Rev.: Comput. Mol. Sci.* **6,** 639-678 (2016).

61. McNaught, A. D. & Wilkinson, A. *IUPAC. Compendium of Chemical Terminology (the "Gold Book")*. 2nd ed. (Blackwell Scientific Publications, Oxford 1997). Online version (2019-) created by Chalk, S. J. https://doi.org/10.1351/goldbook.A00442.
62. Fliegl, H. & Sundholm, D. Aromatic Pathways of Porphins, Chlorins, and Bacteriochlorins. *J. Org. Chem*. **77,** 3408-3414 (2012).
63. Franzke, Y. J., Sundholm, D. & Weigend F. Calculations of current densities and aromatic pathways in cyclic porphyrin and isoporphyrin arrays. *Phys. Chem. Chem. Phys.* **19,** 12794-12803 (2017).
64. Schleyer, P. v. R. & Jiao, H. What is aromaticity? *Pure Appl. Chem*. **68,** 209-21 (1996).
65. Gershoni-Poranne, R. & Stanger, A. Magnetic criteria of aromaticity. *Chem. Soc. Rev*. **44,** 6597-6615 (2015).
66. Lin, Y. C., Jusélius, J, Sundholm, D. & Gauss, J. Magnetically induced current densities in Al_4^{2-} and Al_4^{4-} species studied at the coupled-cluster level. *J. Chem. Phys.* **122,** 214308 (2005).
67. Nava, P., Sierka, M. & Ahlrichs, R. Density functional study of palladium clusters. *Phys. Chem. Chem. Phys.* **5,** 3372-3381 (2003).
68. Franzke, Y. J., Spiske, L., Pollak, P. & Weigend, F. Segmented Contracted Error-Consistent Basis Sets of Quadruple-ζ Valence Quality for One- and Two-Component Relativistic All-Electron Calculations. *J. Chem. Theory Comput.* 16, 5658-5674 (2020).
69. Becke, A. D. Density-functional thermochemistry. III. The role of exact exchange. *J. Chem. Phys.* **98,** 5648-5652 (1993).
70. Lee, C., Weitao, Y. & Parr, R. G. Development of the Colle-Salvetti correlation-energy formula into a functional of the electron density. *Phys. Rev. B* **37,** 785-789 (1988).
71. Yanai, T., Tew, D. P. & Handy, N. C. A new hybrid exchange–correlation functional using the Coulomb-attenuating method (CAM-B3LYP). *Chem. Phys. Lett.* **393,** 51-57 (2004).